


















DEIMOS spectroscopy of $z = 6$ protocluster candidate in COSMOS – A massive protocluster embedded in a large scale structure?

Malte Brinch, ^{1,2*} Thomas R. Greve, ^{1,2,3} David B. Sanders, ⁴ Conor J. R. McPartland, ^{1,4,5,6}
Nima Chartab, ⁷ Steven Gillman, ^{1,2} Aswin P. Vijayan, ^{1,2} Minju M. Lee, ^{1,2} Gabriel Brammer, ^{1,5}
Caitlin M. Casey, ⁸ Olivier Ilbert, ⁹ Shuowen Jin, ^{1,2} Georgios Magdis, ^{1,2,5,10} H. J. McCracken, ¹¹
Nikolaj B. Sillassen, ^{1,2} Sune Toft, ^{1,5} Jorge A. Zavala, ¹²

¹Cosmic Dawn Center (DAWN)

²DTU-Space, National Space Institute, Technical University of Denmark, Elektrovej 327, 2800 Kgs. Lyngby, Denmark

³Department of Physics and Astronomy, University College London, Gower Street, London WC1E 6BT, United Kingdom

⁴Institute for Astronomy, University of Hawaii, 2680 Woodlawn Drive, Honolulu, HI 96822, USA

⁵Niels Bohr Institute, University of Copenhagen, Jagtvej 128, 2200 Copenhagen, Denmark

⁶Physics and Astronomy Department, University of California, 900 University Ave., Riverside, CA 92521, USA

⁷The Observatories of the Carnegie Institution for Science, 813 Santa Barbara St., Pasadena, CA 91101, USA

⁸Department of Astronomy, The University of Texas at Austin, Austin, TX, USA

⁹Aix Marseille Univ, CNRS, CNES, LAM, Marseille, France

¹⁰Institute for Astronomy, Astrophysics, Space Applications and Remote Sensing, National Observatory of Athens, 15236 Athens, Greece

¹¹Institut d'Astrophysique de Paris, UMR 7095, CNRS, and Sorbonne Universit ´e, 98 bis boulevard Arago, 75014 Paris, France

¹²National Astronomical Observatory of Japan, 2-21-1 Osawa, Mitaka, Tokyo 181-8588, Japan

Accepted XXX. Received YYY; in original form ZZZ

ABSTRACT

We present the results of our *Keck/DEIMOS* spectroscopic follow-up of candidate galaxies of r-band-dropout protocluster candidate galaxies at $z \sim 6$ in the COSMOS field. We securely detect Lyman- α emission lines in 14 of the 30 objects targeted, 10 of them being at $z = 6$ with a signal-to-noise ratio of 5 – 20, the remaining galaxies are either non-detections or interlopers with redshift too different from $z = 6$ to be part of the protocluster. The 10 galaxies at $z \approx 6$ make the protocluster one of the richest at $z > 5$. The emission lines exhibit asymmetric profiles with high skewness values ranging from 2.87 to 31.75, with a median of 7.37. This asymmetry is consistent with them being Ly α , resulting in a redshift range of $z = 5.85 - 6.08$. Using the spectroscopic redshifts, we re-calculate the overdensity map for the COSMOS field and find the galaxies to be in a significant overdensity at the 4σ level, with a peak overdensity of $\delta = 11.8$ (compared to the previous value of $\delta = 9.2$). The protocluster galaxies have stellar masses derived from BAGPIPES SED fits of $10^{8.29} - 10^{10.28} M_{\odot}$ and star formation rates of $2 - 39 M_{\odot} \text{ yr}^{-1}$, placing them on the main sequence at this epoch. Using a stellar-to-halo-mass relationship, we estimate the dark matter halo mass of the most massive halo in the protocluster to be $\sim 10^{12} M_{\odot}$. By comparison with halo mass evolution tracks from simulations, the protocluster is expected to evolve into a Virgo- or Coma-like cluster in the present day.

Key words: High-redshift galaxy clusters(2007) — Galaxy evolution(594) — Large-scale structure of the universe(902)

1 INTRODUCTION

Galaxy clusters are the most massive gravitationally-bound virialised objects in the Universe. While star formation activity and stellar mass build-up in clusters must have peaked at earlier times ($z \gtrsim 2$) (following the results of Poggianti et al. 1999; Elbaz et al. 2007; Cooper et al. 2008; Scoville et al. 2013), we do not know how and when

such protoclusters appeared, nor how they affected the formation and evolution of galaxies within them (e.g., Overzier 2016). Studies of present-day galaxy clusters have had some success in addressing these questions, but are limited by the fact that key signatures of a cluster’s formation history are erased in its final stage of assembly as it undergoes dynamical relaxation and virialization (Zabludoff et al. 1996; Kodama et al. 2001).

To better understand the emergence of clusters, we need to study their progenitors (i.e., protoclusters) in the distant Universe, where

* E-mail: malbr@space.dtu.dk

we can directly observe them during their formative stages. Observations must be pushed back to the Cosmic Dawn era ($z \gtrsim 6$), when the Universe was less than a billion years old, since according to state-of-the-art simulations of cosmic structure formation (e.g., Chiang et al. 2013; Chiang et al. 2017; Lovell et al. 2021), protoclusters were assembled from the peaks of dark matter density distribution during the Cosmic Dawn. Simulations suggest that protoclusters form in an "inside-out" manner, where the central galaxies sitting in more massive dark matter halos form first, and then the outer parts form later. Consequently, we expect the central galaxies to be more massive and to have an older stellar population and higher gas-phase metallicity than the outer galaxies.

Overdensities of galaxies at $z \sim 6$ and beyond have been observed in increasingly large numbers in the last few years (e.g., Harikane et al. 2019; Brinch et al. 2023). While such galaxy overdensities are possible protoclusters that will eventually evolve into today's massive galaxy clusters, unambiguous spectroscopic confirmation is essential to establishing these overdensities as genuine protoclusters. It has been demonstrated that a couple of nights (8-16 hours) of deep spectroscopy on 8 – 10 m-class telescopes can confirm the spectroscopic redshift of galaxies out to $z \sim 7$ (Stanway et al. 2004; Stark et al. 2011). To date, however, little more than a handful of spectroscopically confirmed protoclusters at $z \gtrsim 6$ have been found (e.g., Toshikawa et al. 2012, 2014; Chanchaiworawit et al. 2019; Harikane et al. 2019; Hu et al. 2021; Endsley & Stark 2022; Laporte et al. 2022; Helton et al. 2023; Scholtz et al. 2023; Tacchella et al. 2023), and very few of these have the deep multi-band optical/near-IR (OIR) data required to accurately characterize their galaxy populations (e.g., stellar masses, star-formation rates, and ages). Properly constraining the stellar mass of the protocluster galaxies is essential, as it directly ties into the estimation of the dark matter halo mass of the protocluster, which is one of the key pieces of evidence pointing towards these structures evolving into present-day clusters (e.g., Long et al. 2020; Shuntov et al. 2022; Brinch et al. 2023). With the launch of the James Webb Space Telescope (JWST) and large-scale surveys like COSMOS-WEB (Casey et al. 2022), it is possible to search for overdensities at even higher redshifts and with the possibility of spectroscopic follow-up with instruments like NIRSpect (see Laporte et al. 2022; Helton et al. 2023).

In this paper, we present spectroscopic follow-up observations with *Keck* of a protocluster candidate at $z = 6$, first discovered by Brinch et al. (2023). We present spectroscopic confirmation of 10 protocluster galaxies, which allows us to unambiguously confirm that the structure is one of the most massive and galaxy-rich protoclusters known in the Cosmic Dawn epoch. Moreover, it has a well-characterised galaxy population due to unprecedented OIR multi-wavelength data.

The paper is organised as follows. Section 2 discusses how the protocluster candidate galaxies were selected and followed up with the DEep Imaging Multi-Object Spectrograph (*DEIMOS*) instrument on the *Keck* telescope. We further describe the data reduction of the 1-D and 2-D spectra in section 2. Section 3 presents the emission line fitting routine and characterisation of the galaxy spectra, how the quality of each spectrum was graded and the distribution of parameters from the line fit. Section 4 discusses the implications of the protocluster in the wider context of protocluster and galaxy evolution, showing an updated overdensity map updated with new weights given the spectroscopic redshifts and updated estimates for parameters such as stellar mass and star formation rate. Section 5 presents our conclusions.

Throughout the paper, we have adopted a standard Λ CDM cosmology with $H_0 = 70 \text{ km s}^{-1} \text{ Mpc}^{-1}$, $\Omega_m = 0.3$, and $\Omega_\Lambda = 0.70$.

All magnitudes are expressed in the AB system (Oke 1974). A Chabrier (2003) stellar Initial Mass Function (IMF) is used to present our results. The results are reported with 68% confidence interval uncertainties.

2 TARGET SELECTION, OBSERVATIONS AND DATA REDUCTION

2.1 Target selection

The photometric selection of candidate sources was made based on the results of the overdensity analysis done in the COSMOS field (Brinch et al. 2023) using the COSMOS2020 catalogue (Weaver et al. 2022), with LEPHARE (Ilbert et al. 2006) photometric redshifts. We identified a significantly overdense ($\delta_{\text{peak}} = 9.2$, where $\delta = \frac{\Sigma - \langle \Sigma \rangle}{\langle \Sigma \rangle}$ and Σ is the galaxy surface density) and galaxy-rich (19 galaxies) protocluster candidate within a (photometric) redshift bin of $z = 6.05 \pm 0.1$. The 19 galaxies that make up the overdensity, hereafter referred to as PCz6.05-1, were the main targets of our spectroscopic follow-up. *DEIMOS*, being a multiobject spectrometer, allows us to have up to 130 slitlets. To maximize the utility of *DEIMOS*, we included a number of extra sources in our sample.

Our target selection is divided into three separate categories under the following criteria:

Priority 1: The 19 protocluster candidate galaxies found in Brinch et al. (2023).

Priority 2: Galaxies that are also in the $z = 6.05 \pm 0.1$ redshift bin and within the *DEIMOS* footprint but outside the 4σ overdensity contour. These targets constitute five sources in total.

Priority 3: Galaxies obtained by increasing the size of our redshift bin size to $\Delta z = \pm 0.5$ and by relaxing the sample selection criteria we had in Brinch et al. (2023), letting the galaxies inside the bin have their maximum $p(z)$ value deviate more than 5% of their median value. These targets constitute six sources in total.

On top of this, some slits have multiple sources on them, we report these extra serendipitous sources in appendix ???. There were 8 extra sources found on our slits. In total, we have 30 sources across our three priorities. For the priority 1 sources, 14 of them are classified as i-dropouts according to the criteria in Ono et al. (2017), with $K_s = 25.08 - 28.08$ mag. The remaining slitlets were used to target other lower redshift galaxies. The many filters that have been used to observe the COSMOS field allow for well-characterised spectral energy distribution (SEDs) with well-constrained photometric redshifts, resulting in a high probability that the protocluster candidate galaxies are close to their median photometric redshift.

2.2 Observations

The spectroscopic follow-up was performed using the DEep Imaging Multi-Object Spectrograph (*DEIMOS*; Faber et al. 2003) at the Nasmyth focus of the 10 m *Keck* II telescope. Observations took place on 2022 February 6 – 7 UT, with all our Priority 1 – 3 targets observed. The seeing was in the range $0''.75 - 1''.00$. Two *DEIMOS* masks were used to observe the targets, one for each night, as seen in Table 1. The first mask H250-1 used the OG550 filter and the 900 lines mm^{-1} grating (900ZD), with a blaze wavelength of 5500 \AA , tilted to place

Table 1. Summary of observation with *Keck/DEIMOS* in the COSMOS field.

Mask ID	Date (UT)	Exp time [s]	N ^a	Grating [mm ⁻¹]	λ_{central} [Å]	Filter	Seeing ^b [arcsec]
H250-1	2022 Feb 7	24000	11	900	8000	OG550	1
H250-2	2022 Feb 8	25200	19	600	7500	OG550	0.75

^a Number of observed targets.

^b Average seeing over the night.

a central wavelength of 8000 Å on the detectors. This configuration provided a spectral coverage between 6193.8 Å and 9799.6 Å. The second mask H250-2 used the OG550 filter and the 600 lines mm⁻¹ grating (600ZD), with a blaze wavelength of 7500 Å, tilted to place a central wavelength of 7500 Å on the detectors. This configuration provided a spectral coverage between 5500.0 Å and 10118.9 Å. The spatial pixel scale was 0''.1185 pixel⁻¹ (0.68 kpc pixel⁻¹ at $z=6$), with spectral dispersion of 0.44 Å pixel⁻¹ (16 km s⁻¹ pixel⁻¹) for the 900 lines mm⁻¹ and 0.65 Å pixel⁻¹ (16 km s⁻¹ pixel⁻¹) for the 600 lines mm⁻¹ grating. Slit widths were 1''. The FWHM resolution for the 900ZD was ≈ 2.1 Å and ≈ 3.1 Å for the 600ZD grating (74 km s⁻¹ and 109 km s⁻¹ respectively for a Lyman- α line at $z = 6$). The specifics of the *DEIMOS* observations are detailed in Table 1¹.

2.3 Data Reduction

The *DEIMOS* slits are constructed as a blue-red pair between two detectors, with four pairs in total. For the reduction of the *DEIMOS* spectra, *PyPeIt*² (Prochaska et al. 2020a; Prochaska et al. 2020b), a PYTHON package for semi-automated reduction of astronomical slit-based spectroscopy was used. The individual observations of each 2-D slit were reduced by *PyPeIt* (including coadding) and then fluxed calibrated to convert the units from counts to 10⁻¹⁷ erg/s/cm². Then each slit was visually inspected for possible sources. To flag sky regions, which can affect the detection of sources on the slit, we locate noise spikes in the 1-D spectrum that are equal to or larger than the FWHM resolution of *DEIMOS*, which are indicative of sky regions. Data in sky regions are masked when fitting potential emission lines, except in cases where there is a strong detection within a sky region that extends beyond it so that there is no ambiguity as to whether or not the detection is due to a sky region. The flagged sky regions were also checked against the skylines from Rousselot et al. (2000), with vacuum line wavelengths computed from laboratory data and a spectra range 0.997-2.25 μm with a resolution of $R \sim 8000$. Slits can have multiple detections that are not part of our original sample. To identify our main targets, as well as all other sources in the slit, we construct true-colour RGB images of the Y, z, i and K, H, J bands with the *DEIMOS* slit overplotted. We also compare this to galaxies in the COSMOS2020 catalogue to determine the counterpart of each source detected in the slits. The true color images are found next to each spectrum for comparison (see for example figure 2). The 1-D spectra were manually extracted by collapsing the spectra around the 2-D line observation. This was done to account for the multiple objects in the slits. The noise is calculated as the RMS of all the pixels in each column that are not part of the pixels used to create the signal for the 1-D spectra (i.e. away from the sky and emission lines). If there are multiple sources on the slit, they are masked when calculating the noise.

¹ More info about *DEIMOS* can also be found at <https://www2.keck.hawaii.edu/inst/DEIMOS/specs.html>.

² <https://pypeit.readthedocs.io/en/latest/>

3 RESULTS & ANALYSIS

With the spectroscopic data reduced, we now turn to fitting the Lyman- α lines to determine their characteristics and the galaxies' redshifts. The Lyman- α emission line is associated with the hydrogen atom and is emitted when an electron transitions from an excited state ($n = 2$) to the ground state ($n = 1$), with a rest frame wavelength of 1216 Å. The emission line is used to observe distant galaxies due to its relatively high line strength, which comes from Star-forming galaxies that produce huge amounts of Lyman- α photons by recombination in HII regions that are ionised by young stars (Tapken et al. 2007).

3.1 Emission line fitting

The Lyman- α line profile at $z \sim 6$ is expected to be observed as one of two profiles (Childs & Stanway 2018; Calvi et al. 2019; Mason & Gronke 2020). The shape of the Lyman- α line profile arises due to the path Lyman- α photons take to escape their local environment. As the photons travel they experience strong resonant scattering from neutral hydrogen in the interstellar medium (ISM) and circumgalactic medium (CGM). The scattering through an optically thick cloud of HI gas means only the blue- and red-shifted emission is observed leading to a double-peaked Gaussian line profile, with the central wavelength being strongly absorbed and re-scattered. It is expected that the blueward peak of the profile is lower than the redward one, due to the intervening Inter Galatic Medium (IGM) between us and the galaxy. It is possible for the blue part of the line to be preferentially absorbed, or for the red part to be boosted by back-scattering from an expanding medium. The resulting line profile in that case is an asymmetric P-Cygni or more generally skewed Gaussian line profile. The skewed Gaussian is parameterised using the following formula,

$$f(x; A, \mu, \sigma, \gamma) = \frac{A}{\sigma\sqrt{2\pi}} e^{-(x-\mu)^2/\sigma^2} \left\{ 1 + \text{erf} \left[\frac{\gamma(x-\mu)}{\sigma\sqrt{2}} \right] \right\}, \quad (1)$$

with erf() being the error function and the four parameters being the Amplitude (A), centre (μ), sigma (σ) and skew (γ). We expect the skew from the fit to be positive due to the attenuation in the blue part of the line (Calvi et al. 2019). Note that in the case of zero skew, the skewed Gaussian becomes a standard Gaussian. We use the LMfit package (Newville et al. 2014) to fit the emission lines, which uses a form of least-squares fitting. To test whether there is significant continuum detection in conjunction with line detection, a linear baseline is fitted together with the emission line profile(s). For all the detections except two, the line fits have no continuum detection above the noise. The spectra were also visually inspected to check for any continuum detection between the Lyman α line and the supposed Lyman break given the redshift of each object.

To accurately quantify the uncertainty on the emission-line fitting, we apply Monte Carlo (MC) sampling (Kroese & Rubinstein 2011), with N=1000 iterations³. The noise at each wavelength is used to sample Gaussian noise which is then added to each individual flux value before the lines are fit. This is done N times to obtain a distribution of line widths and fluxes. We report the median, upper and lower 1 σ (68%) confidence interval for the MC sampling results.

It is important to note for the skewed Lyman- α line profile that the wavelength obtained when fitting, and consequently the redshift, will be at the position of the lower wavelength edge (as

³ Higher iteration counts were tested and gave virtually identical results.

marked by the blue lines in Figure 2) and not at the centre of the measured line flux. Since the line is asymmetrically attenuated, it is not possible to know how much of the line is attenuated and hence where the true wavelength centre of the un-attenuated line would be. This means that there is a possibility that the redshift of the galaxy is lower. The error reported in Table 3 is from the line fitting and does not include inherent negative uncertainty due to the nature of the skewed Lyman- α line profile.

3.2 Final Spectra

To determine the quality of the final spectra as seen in Figures 2-4, we adopt the – excellent (A), acceptable (B), marginal (C) and non-detection (D) categories, adapted from Calvi et al. (2019). The grading criteria were based on

- (1) the shape of their spectra resembling either a P-Cygni or double-peaked Gaussian profile in the 1D spectra;
- (2) the sizes of Ly α emission features are about 1 arcsec (\sim seeing of a spectroscopic night), but neither too extended nor too compact in 2D (to discern the real detection from the sky and cosmic ray residuals)
- (3) The locations of emission lines are fairly far away from strong sky emission lines or their wings.

If a detection satisfies all of the three criteria, it is given the letter grade ‘A’. If a detection fails any one criterion, it is given grade ‘B’. If a detection fails two criteria it is given the grade ‘C’. If a detection fails all three criteria, or no detection is found on the slit, the source is labeled as a non-detection and is given grade ‘D’. For a line to be considered a detection, its peak signal-to-noise has to be above 3σ . Every line is also checked to see whether it is larger than the FWHM resolution of the instrument and treated as a non-detection if this is not the case. In total we found 3 grade A (Figure 2), 7 grade B (Figure 3) and 2 grade C (Figure 4) sources at $z \approx 6$. Sources that are interlopers are shown in appendix ???. We chose not to include the redshifts from grade C detections in our further analysis due to their uncertainty.

3.3 Spectroscopic Protocluster membership

The 10 galaxies have a median redshift of $z = 5.98$ and a $\Delta z = 0.23$. It should be noted that 2/10 galaxies are situated outside the main overdensity peak (see Figure 6). We address the size of Δz in §4.5. The remaining sources are either grade C detections or interlopers where the redshift deviates too much from $z = 6$ to be part of the protocluster or non-detections.

Overall 14/30 (47%) of the galaxies had a grade A/B detection. Figure 1 shows a comparison with the photometric redshift from LEPHARE. We have chosen not to show the grade C detections in this plot, due to their uncertainty.

3.3.1 Low- z objects

The [OIII] lines at 4959 Å, 5007 Å, as well as the [OII] doublet at 3927 Å, 3929 Å and H β 4861 Å line for galaxies at $z \sim 1$ fall within the wavelength range probed by DEIMOS. The [OIII]5007Å line is expected to be the brightest, while the [OII]4959Å line is expected to be $\sim 3\times$ fainter (Storey & Zeippen 2000). Meanwhile the [OII] doublet around 3928 Å can look similar to a double peaked Lyman- α profile. We would like to highlight a potential candidate for such a low- z interloper in galaxy 70505 and explain why we believe it to

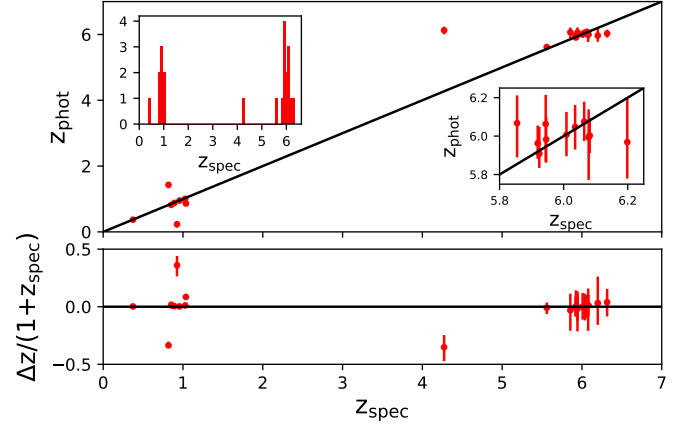


Figure 1. Comparison between the photometric redshift from LEPHARE and the spectroscopic redshift from the DEIMOS campaign. The inset in the upper left panel shows the histogram of spectroscopic redshifts for all detections, while the lower right panel shows a zoom-in at $z \approx 6$. The lower panel shows the residuals $\Delta z / (1 + z_{\text{spec}})$, where $\Delta z = z_{\text{spec}} - z_{\text{phot}}$.

be a genuine high- z detection. Firstly, if the two peaks that appear to be present were due to [OII], we should expect their peaks to be separated by ≈ 3 Å rest frame, and the galaxies redshift would be $z = 1.26$ meaning the peaks should be separated by 6.3 Å observed frame. Given that the separation is 5.7 Å, it leads us to conclude that it is not the [OII] doublet. Secondly, since one part of the line is over a skyline, there is a part of the 2D spectrum which is over-subtracted. This leads to a dip in the 1D spectrum when collapsed, which can make it appear as if the line is two lines. For these reasons, we have chosen to set the line as a Lyman- α detection and to extrapolate over the missing part of the line. It is possible that we are missing flux from the fit, though this should not affect the determination of the spectroscopic redshift. Generally, it is important to keep these lines in mind when investigating other sources found within the slit. The spectroscopic redshifts of these low redshift galaxies are shown in appendix ??? and Figure 1.

3.4 Ly- α Line Characteristics

Figure 5 shows the distribution of the Lyman- α emission line properties for the emission lines we have detected. The flux range is $F = 0.63 - 6.79 \times 10^{-18} \text{ erg s}^{-1} \text{ cm}^{-2}$ with a median of $F_{\text{med}} = 1.09 \times 10^{-18} \text{ erg s}^{-1} \text{ cm}^{-2}$ and the corresponding luminosity range is $L = 0.246 - 2.628 \times 10^{42} \text{ erg s}^{-1}$ with a median of $L_{\text{med}} = 0.431 \times 10^{42} \text{ erg s}^{-1}$. We find that the peak signal-to-noise of the line detection for these 10 sources is between 5 – 20.

Many of the sources we observe show no clear continuum detection above the noise. In those cases we calculate the 2σ lower limit for the equivalent width as follows,

$$\text{EW}_{0, \text{Ly}\alpha}^{\text{lower}} = \frac{1}{1+z} \times \frac{F_{\text{Ly}\alpha}}{f_{\text{cont}}^{2\sigma}}, \quad (2)$$

where $\text{EW}_{0, \text{Ly}\alpha}^{\text{lower}}$, $F_{\text{Ly}\alpha}$, z , $F_{\text{Ly}\alpha}$, and $f_{\text{cont}}^{2\sigma}$ are the lower limit of Ly- α restframe equivalent width, redshift of a galaxy, total Ly- α emission flux, and the 2σ non-detected flux density level, respectively. We measured the value of $f_{\text{cont}}^{2\sigma}$ by averaging 2σ RMS noise levels $\sim 50 - 100$ Å redward of the Ly- α emission lines. In the case where there is a sufficiently high continuum above the noise, we

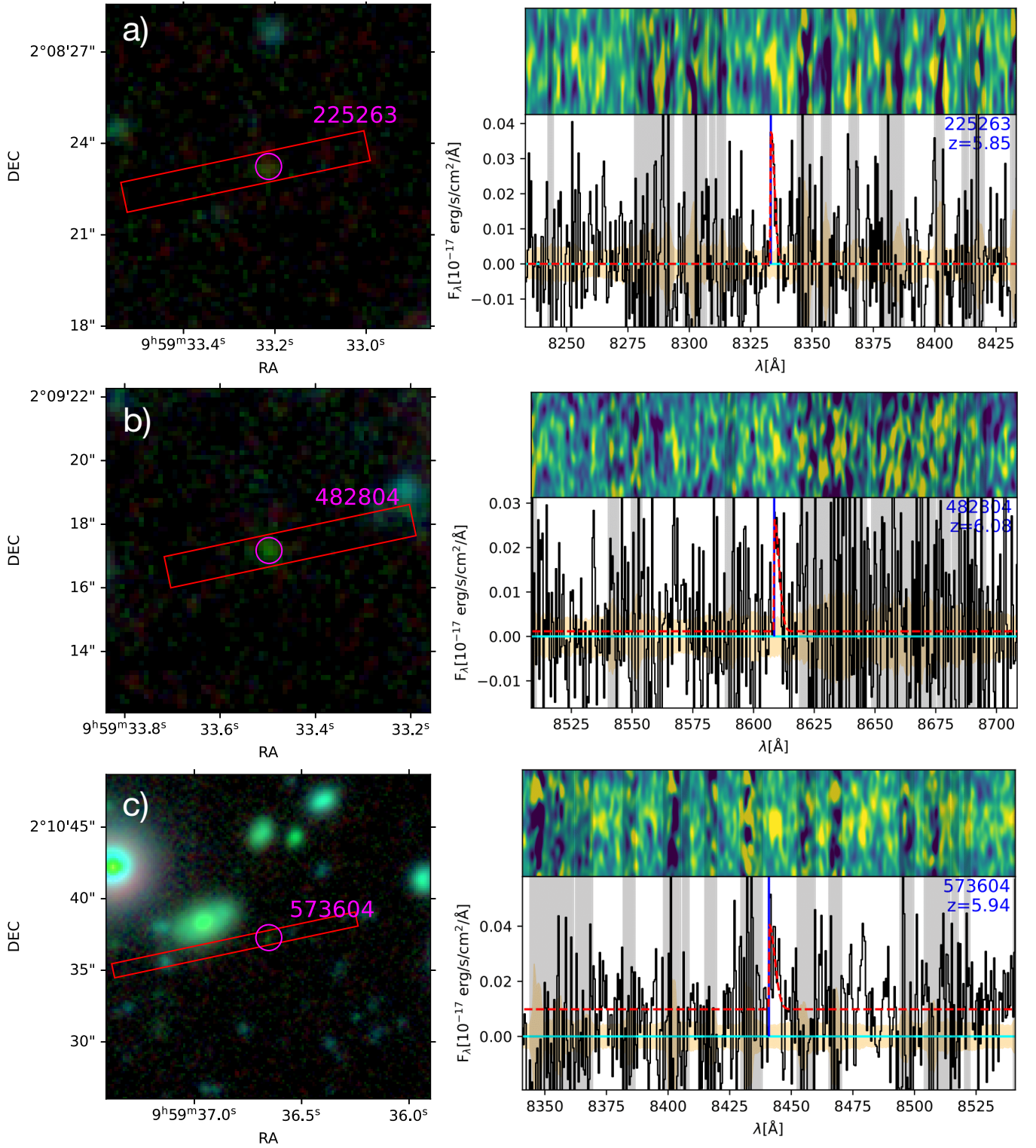


Figure 2. 2D, 1D and Yzi RGB true-colour images of the protocluster members with grade A as seen in Table 3. The left side shows VISTA Yzi RGB true colour images using the COSMOS2020 catalogue photometry. The slit used to observe each object is plotted on top of the image and a magenta circle with an accompanying object ID is shown to highlight the position of the object in the image. The right side shows a two-panel figure of the spectrum in 2D (top), and 1D (bottom). A Gaussian filter has been applied to the 2D spectrum to visually highlight the detection. The black solid line is the extracted 1D spectrum. The vertical blue line indicated the spectroscopic redshift of the object. The shaded yellow area is the noise. The grey-shaded regions in all three panels highlight the sky regions, where skylines are prevalent.

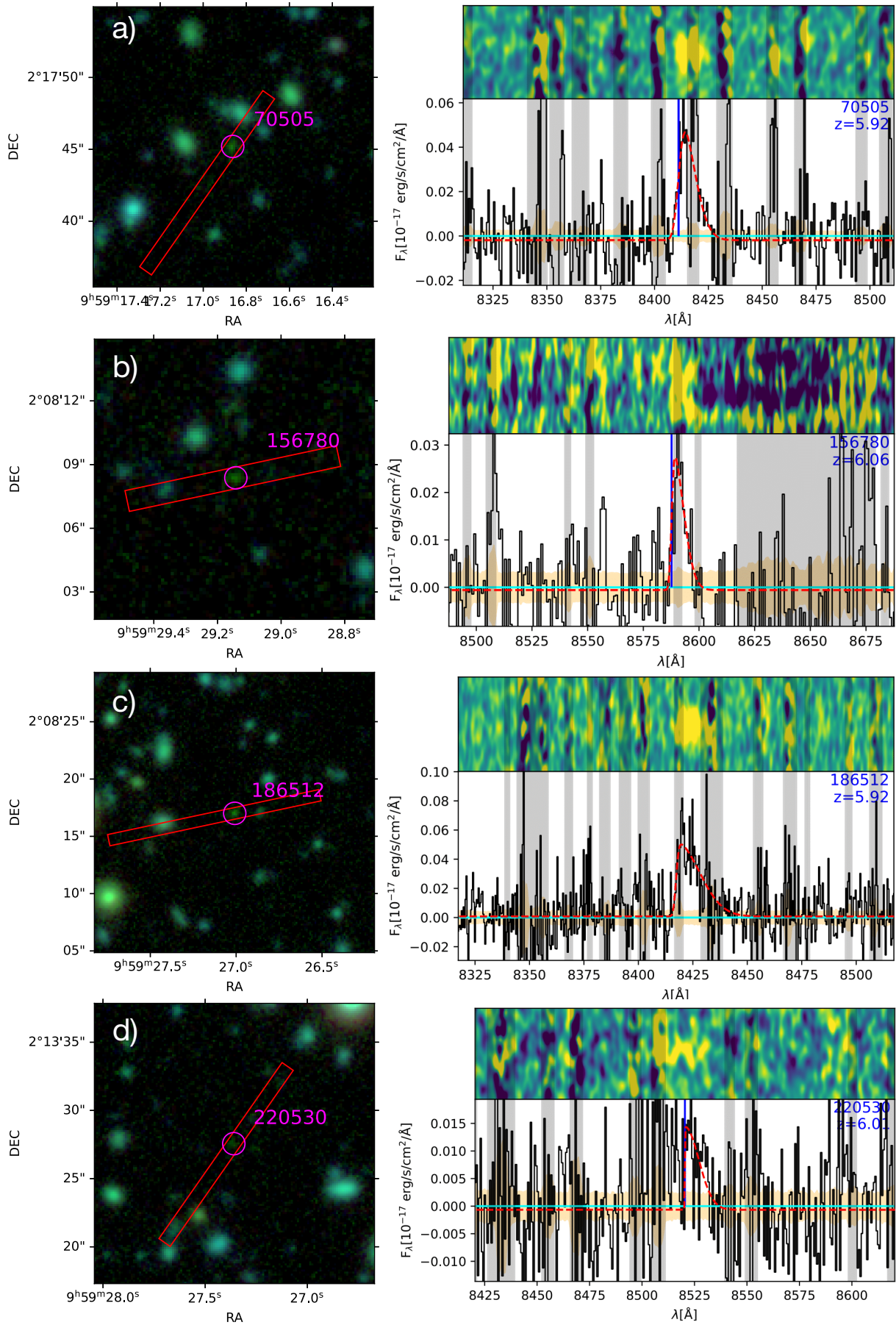


Figure 3. Continued on the next page.

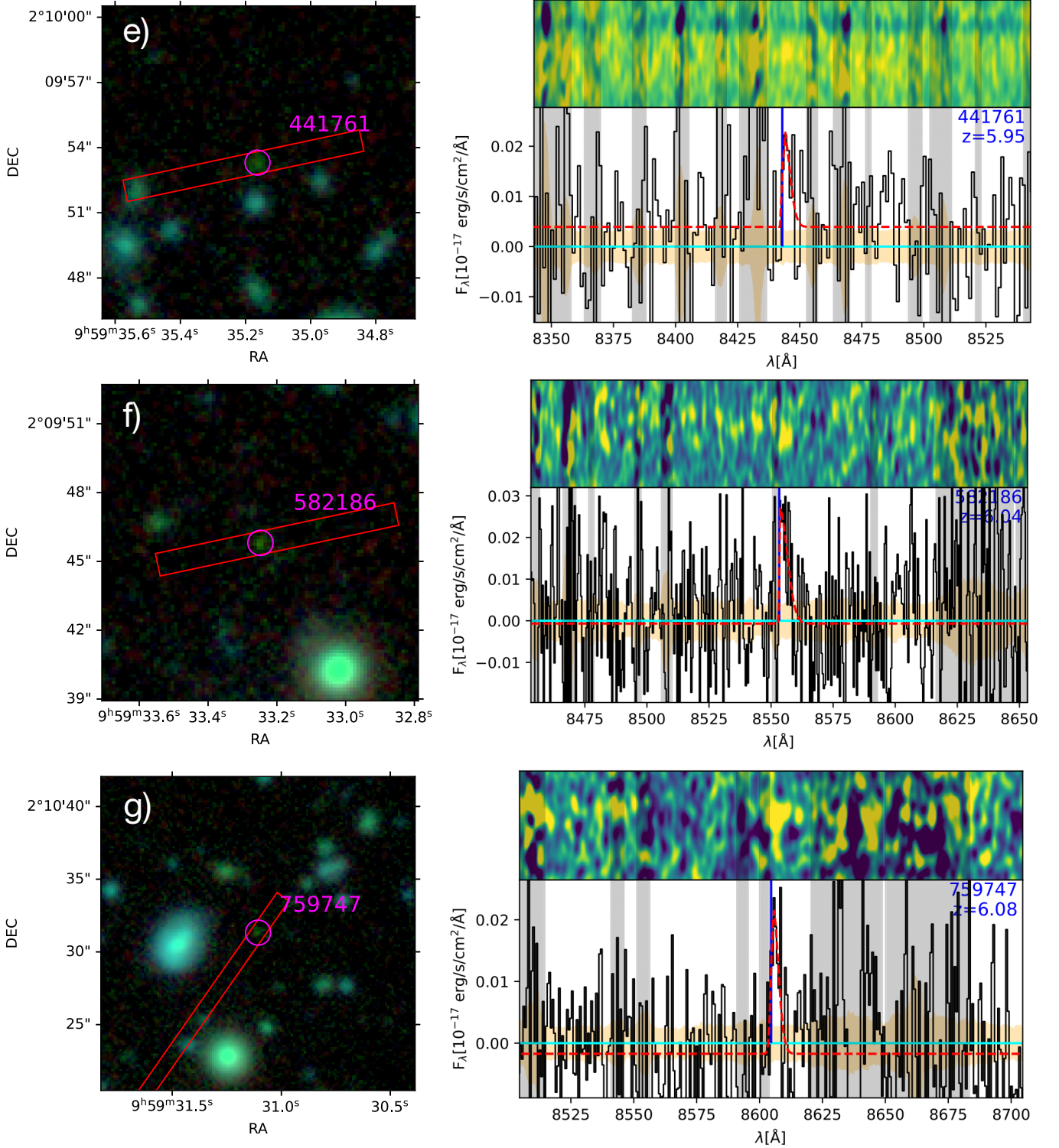


Figure 3. Same as Figure 2 but for those protocluster members ranked B.

calculate the equivalent width using the average continuum flux, $f_{\text{cont}}^{\text{avg}} \sim 50 - 100 \text{ \AA}$ redward of the line instead. Two of the $z = 6$ protocluster galaxies have a continuum above the noise, 441761 and 573604 (see table 4). Their equivalent widths are 3 \AA and 1 \AA , respectively. We have chosen to compare their 2σ lower limit, to consistently compare with the other sources. The distribution of the

equivalent width lower limits are shown in Figure 5c. We find an EW range of $1 - 16 \text{ \AA}$ with a median of 2 \AA . None of the detections would definitively qualify the objects as being Lyman alpha emitters (LAEs), since that would require $\text{EW} > 20 \text{ \AA}$ (Guaita et al. 2015). This does not mean that the galaxies are not LAEs, but rather that our observations are not deep enough to draw this conclusion. The

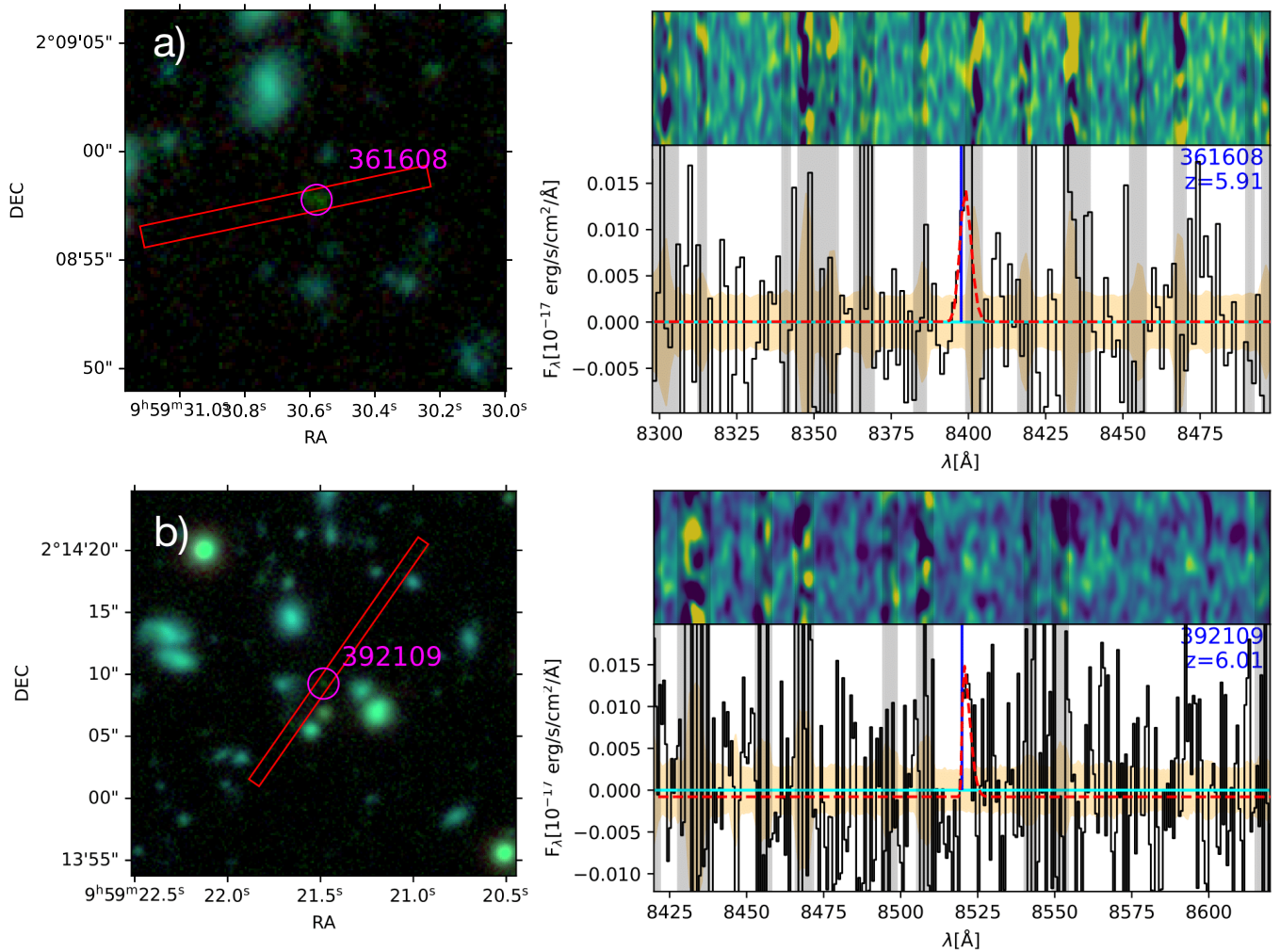


Figure 4. Same as Figure 2 but for those protocluster members ranked C.

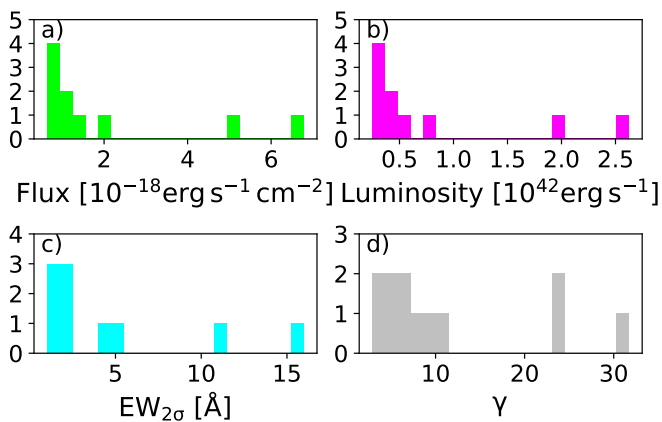


Figure 5. Histograms showing the distribution of **a)** Ly α fluxes, **b)** Ly α luminosities, **c)** 2σ lower limits on the equivalent widths, and **d)** line skewness parameters.

EW > 20 Å cutoff between Lyman break galaxies (LBGs) and LAEs is also debated (Kerutt et al. 2022).

Finally, the gamma (skew) distribution for our detection has a range of 2.87 – 31.75 with a median of 7.37. Since we expect the skewed Ly α line to have a positive skew, it leads further credence to the validity of the detection that all of them are significantly positively skewed. It should also be noted that while the uncertainty on the determination of the skew tends towards being large (see Table 3), the uncertainty tends towards higher values, not lower or negative values. An important point to keep in mind when fitting a skewed Gaussian is that the skew value is sensitive to the binning and it is possible to get both positive and negative values for the skew depending on the amount of binning done. Therefore, we have chosen not to bin the data for any of the grade A and B detection, to not bias our skew values.

For comparison, Calvi et al. (2019) did multi-object spectroscopy using OSIRIS at the *Gran Telescopio Canarias* of 16 LAE candidates discovered in the *SubaruXMM Newton Deep Survey* as part of a $z \sim 6.5$ protocluster candidate. Compared to the galaxies studied in Calvi et al. (2019), their sources are generally brighter, more luminous and broader (higher EW) than our galaxies, with the skew being comparable. It should be noted that their OSIRIS observation has $\sim 3\times$ the amount of observation time as our objects. Given that none of their and few of our objects have continuum

detections it makes sense that their observations are generally brighter and broader since they have had more time to uncover more of the line flux.

4 DISCUSSION

4.1 A revised overdensity estimate of PCz6.05-1

Given our new spectroscopic redshifts, we can calculate an improved estimate of how overdense of an environment PCz6.05-1 resides in. We do this by re-creating an overdensity map with updated weights, following the Weighted Adaptive Kernel method laid out in [Brinch et al. \(2023\)](#). All galaxies with grade A or B detections will have their redshift updated and their weight set to one. Grade C or D detections will not have their redshift updated and their photometric redshift probability distribution will still be used. To analyse the distribution of overdensities in the COSMOS field we make a redshift bin which includes galaxies whose spectroscopic redshift falls within the bin, as well as galaxies with photometric redshifts that fall within the bin (see [Brinch et al. 2023](#), for a list of selection criteria used). Since the redshift distribution of the spectroscopically confirmed galaxies is skewed slightly lower than the original photometric distribution, we chose a slightly lower centre of $z = 5.97$ for our bin, with a $\Delta z = 0.30$ to incorporate all the galaxies with spectroscopic redshifts around $z = 6$. Figure 6 shows the resulting overdensity map using the spectroscopic redshift, including those from the literature ([Mallery et al. 2012](#); [Hasinger et al. 2018](#); [Casey et al. 2019](#); [Jin et al. 2019](#); [Williams et al. 2019](#); [Zavala 2021](#); [Khostovan et al. 2023](#)). We find that the overdensity associated with PCz6.05-1 has significantly increased, from the previous peak overdensity value of $\delta_{\text{OD}} = 9.2 (8.0\sigma)$ reported in [Brinch et al. \(2023\)](#) to a revised value presented here of $\delta_{\text{OD}} = 11.6 (10.9\sigma)$. This unequivocally puts PCz6.05-1 on par with the most overdense protoclusters identified at these redshifts ([Harikane et al. 2019](#)), although, we caution that overdensity calculations vary across different studies ([Harikane et al. 2019](#), and references therein), making direct comparisons between protoclusters challenging. Richness, that is the number of galaxies in an overdensity, is a simpler and more easily comparable measure between different protocluster studies. There are also indications that richness is among the better tracers of which overdensities will end up as massive ($10^{15} M_{\odot}$) a galaxy cluster at $z = 0$ ([Remus et al. 2022](#)).

4.2 Discovery of a $z \approx 6$ large-scale structure in COSMOS

From Figure 6 it is seen that PCz6.05-1 appears to be embedded in a large-scale structure that spans across the central parts of the COSMOS field. PCz6.05-1 is connected via a filament to an even stronger and more extended overdensity located within the JWST/PRIMER field (ID: 1837; PI: J. Dunlop). This second $z \approx 6$ protocluster is hitherto unknown, and we report its discovery here. Its centroid location is at (RA, DEC) = (150.113°, 2.255°) and it contains 22 galaxies with spectroscopic redshifts within the 4σ overdensity contour. The median spectroscopic redshift of these 22 galaxies is $\bar{z} = 5.89$ with a z -range of $\Delta z = 0.27$. The peak overdensity is $\delta = 12.5 (11.8\sigma)$, i.e., larger albeit comparable to that of PCz6.05-1. The overdensity seems to be made up of at least two more compact ‘cores’, with one containing 13 spectroscopically confirmed galaxies ($\bar{z} = 5.86 \pm 0.07$) and the other with 9 spectroscopically confirmed galaxies ($\bar{z} = 6.01 \pm 0.13$). In addition to these highly significant overdensities and their connecting filaments in the central regions of the COSMOS field, four

smaller, yet significant ($\geq 4\sigma$), overdensity peaks are seen in the lower half of the overdensity map in Figure 6. It is possible that they trace out a large structure that connects to PCz6.05-1 and the second central overdensity in the map. Taking the 1σ contour as a crude measure of the size, the overall structure has an of 84 cMpc across, with 4 peaks in the lower parts of the field indicating the structure could have an even larger extent.

4.3 Properties of the galaxies in PCz6.05-1

4.3.1 SED fitting

To analyse the physical properties of the protocluster galaxies in PCz6.05-1, we employ the Bayesian Analysis of Galaxies for Physical Inference and Parameter ESTimation (BAGPIPES), which is a Bayesian SED fitting code ([Carnall et al. 2018](#)). BAGPIPES allows for the fitting of both photometry and spectra to obtain estimates of physical properties such as stellar mass, star formation rate (SFR), Dust obscuration (A_V) and the mass-weighted age of the galaxy. BAGPIPES also includes the treatment of nebular emission lines from CLOUDY modelling ([Ferland et al. 2013, 2017](#)), which has been shown to be increasingly relevant for high- z galaxies, especially with the advent of JWST ([Endsley et al. 2023](#)). Although BAGPIPES allows for the spectrum to be included as part of the fitting process, it encounters challenges in accurately fitting the Ly α line due to its variable dampening and as a result, we do not include the spectra in the fitting process. The redshifts of the PCz6.05-1 galaxies were fixed to their spectroscopic redshift values. We use the following parameter ranges when fitting: formation mass $\log(M_{\star}) \in [6.0 : 12.0] \log(M_{\odot})$, metallicity $Z \in [0.01 : 2.00] \log(Z_{\odot})$, reddening $A_V \in [0.0 : 4.0]$ (utilizing a [Calzetti et al. \(2000\)](#) dust law) and the U parameter, which is the strength of the nebular radiation field to $\log(U) \in [-4.0 : -1.0]$. To fit the galaxies we use all available FARMER photometry from the COSMOS2020 catalogue, which includes observations from the ultraviolet to the far infrared (see [Weaver et al. \(2022\)](#) for details). BAGPIPES allows for different star formation histories (SFH) when fitting. We tested the following SFHs: constant, double power law, delayed, lognormal, exponential, constant+exponential model and a non-parametric SFH ([Leja et al. 2019](#)). We found that parametric models resulted in an artificially tight relationship for the galaxy main sequence and yielded unrealistic ages, all of which were < 10 Myr. We have, therefore, chosen to use the non-parametric SFH when fitting our galaxies. It is worth noting that [Endsley et al. \(2023\)](#) argue that galaxies, especially those with very young ages ($\lesssim 10$ Myr), tend to produce stellar masses $\sim 0.5 - 1$ dex higher when utilizing a non-parametric SFH with a continuity prior, as opposed to employing a constant SFH. A non-parametric SFH that disfavors extremely rapid changes in SFR, like the continuity prior used in BAGPIPES, can increase the masses up to ≈ 2 dex higher than using a constant SFH with a very young SED age. We argue that the use of a non-parametric SFH is appropriate for our galaxies for several reasons. Firstly, when inspecting the SFH for the constant and non-parametric models for the galaxies with very young ages, all of the star formation for the constant model happens in a single short burst, as opposed to the non-parametric model where the shape of the SFH tends to be lognormal for these galaxies (see Figure appendix ??). Secondly, the stellar mass provided by the non-parametric model is at most 0.5 dex greater, and in most cases 0.2 dex greater. This difference in stellar mass does not change any conclusion in our further analysis. Thirdly, the shape of the non-parametric SFH is akin to a (truncated) log-normal distribution, which is in line with what is found from simulations of high- z galaxies within our mass range ([Wilkins et al. 2023](#)). For these rea-

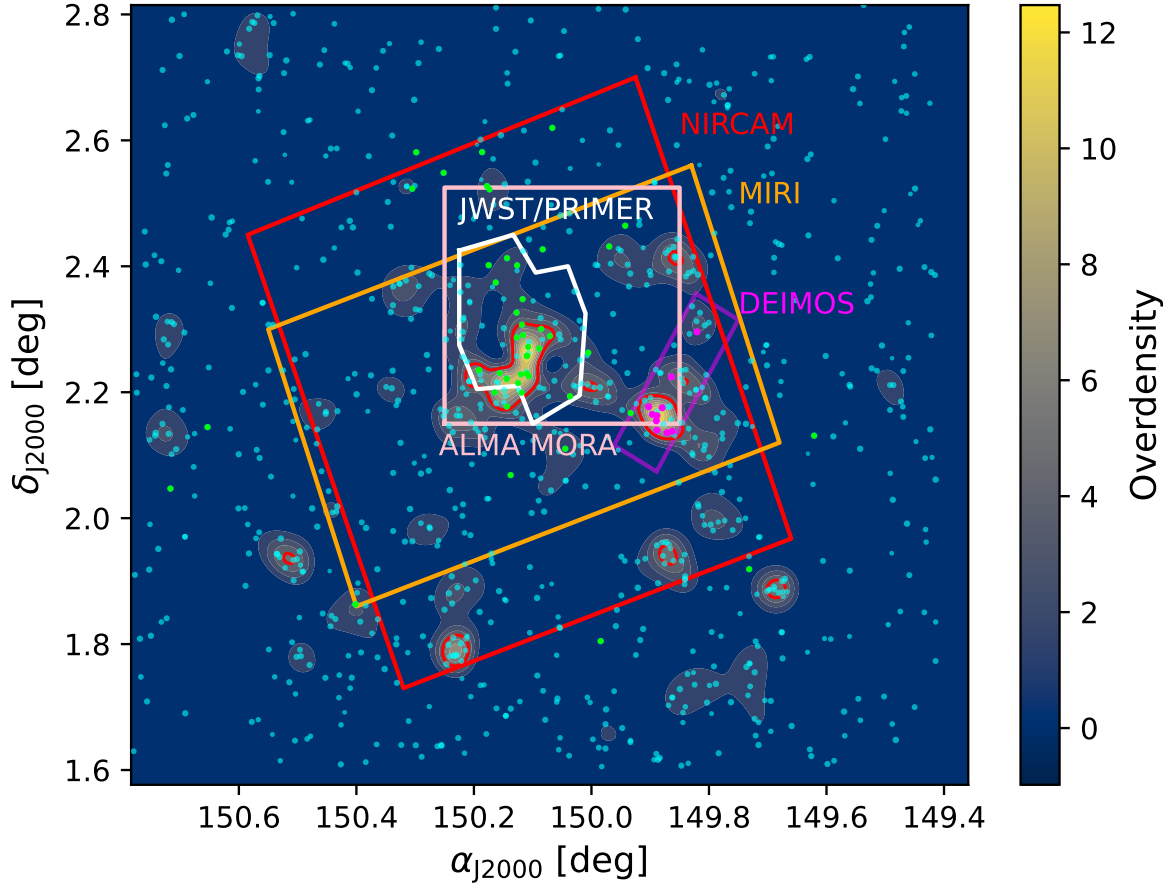


Figure 6. The galaxy overdensity field at $z = 5.97 \pm 0.15$ in COSMOS, derived from the Weighted Adaptive Kernel method described in Brinch et al. (2023). Contours are in steps of 1σ , where σ is calculated as the standard deviation of the overdensity values in the field. The 4σ contours have been highlighted in red. Individual galaxies are indicated as cyan dots, except for the magenta dots which indicate the galaxies with secure (grade A and B) Ly α detections presented in this paper, and the green dots which show other spectroscopically confirmed galaxies within the redshift bin (Mallery et al. 2012; Hasinger et al. 2018; Casey et al. 2019; Jin et al. 2019; Williams et al. 2019; Zavala 2021; Khostovan et al. 2023). The DEIMOS field of view is shown as the magenta rectangle. The JWST/PRIMER (white), ALMA MORA (pink), COSMOS-WEB NIRCAM (red) and COSMOS-WEB MIRI (orange) footprints are also shown.

sons, we have opted to stick with the non-parametric SFH. BAGPIPES fits to the galaxies in PCz6.05-1 are shown in Appendix ??, and the resulting physical properties from their best-fit SED models are listed in Table 2. Overall, there is good agreement with the physical properties presented in Brinch et al. (2023), which were based on SED fits with LEPHARE and without spectroscopic redshifts. The main difference is with the stellar masses where BAGPIPES generally yields somewhat lower masses.

To compare with other galaxies in the field at a similar redshift, we also fit all the galaxies in the $z = 5.97 \pm 0.15$ redshift bin (shown as cyan dots in Figure 6). Because all of our galaxies with spectroscopic redshifts were best fit with a non-parametric SFH, we also adopted this when fitting the galaxies with only photometric redshifts. Assuming that all these galaxies are within the redshift bin, we have therefore opted to fix it to the photometric redshifts from LEPHARE.

Table 2. BAGPIPES results for PCz6.05-1 protocluster galaxies with spectroscopic redshift. Columns: (1) COSMOS2020 catalogue ID; (2) The mass-weighted age; (3) the stellar mass; (4) the star formation rate; (5) reddening using a Calzetti et al. (2000) dust law.

ID	age	$\log M_*/M_\odot$	SFR	A_V	Z
(1)	[Myr]	[dex]	$[M_\odot/\text{yr}^{-1}]$	(5)	$[Z_\odot]$
	(2)	(3)	(4)		(6)
70505	100^{+142}_{-72}	$8.64^{+0.23}_{-0.2}$	3^{+1}_{-1}	$0.29^{+0.05}_{-0.05}$	$0.24^{+0.06}_{-0.03}$
156780	133^{+120}_{-91}	$8.60^{+0.23}_{-0.2}$	3^{+1}_{-1}	$0.36^{+0.06}_{-0.06}$	$0.24^{+0.06}_{-0.04}$
186512	96^{+85}_{-60}	$8.56^{+0.18}_{-0.15}$	3^{+1}_{-1}	$0.04^{+0.04}_{-0.03}$	$0.03^{+0.35}_{-0.01}$
220530	77^{+74}_{-47}	$8.29^{+0.12}_{-0.16}$	2^{+1}_{-1}	$0.04^{+0.04}_{-0.03}$	$0.02^{+0.04}_{-0.01}$
225263	101^{+119}_{-67}	$9.01^{+0.24}_{-0.22}$	8^{+4}_{-2}	$0.75^{+0.05}_{-0.05}$	$0.04^{+0.02}_{-0.01}$
441761	134^{+114}_{-73}	$9.65^{+0.19}_{-0.18}$	35^{+13}_{-9}	$1.11^{+0.04}_{-0.05}$	$0.04^{+0.02}_{-0.01}$
482804	213^{+109}_{-110}	$9.18^{+0.12}_{-0.16}$	8^{+2}_{-2}	$0.28^{+0.12}_{-0.13}$	$0.53^{+0.19}_{-0.18}$
573604	31^{+67}_{-24}	$9.09^{+0.12}_{-0.07}$	12^{+2}_{-1}	$1.08^{+0.04}_{-0.04}$	$0.22^{+0.02}_{-0.01}$
582186	386^{+66}_{-81}	$10.28^{+0.06}_{-0.07}$	39^{+18}_{-13}	$0.73^{+0.15}_{-0.18}$	$1.37^{+0.4}_{-0.48}$
759747	235^{+112}_{-116}	$8.91^{+0.18}_{-0.23}$	4^{+1}_{-1}	$0.24^{+0.11}_{-0.12}$	$0.3^{+0.18}_{-0.11}$

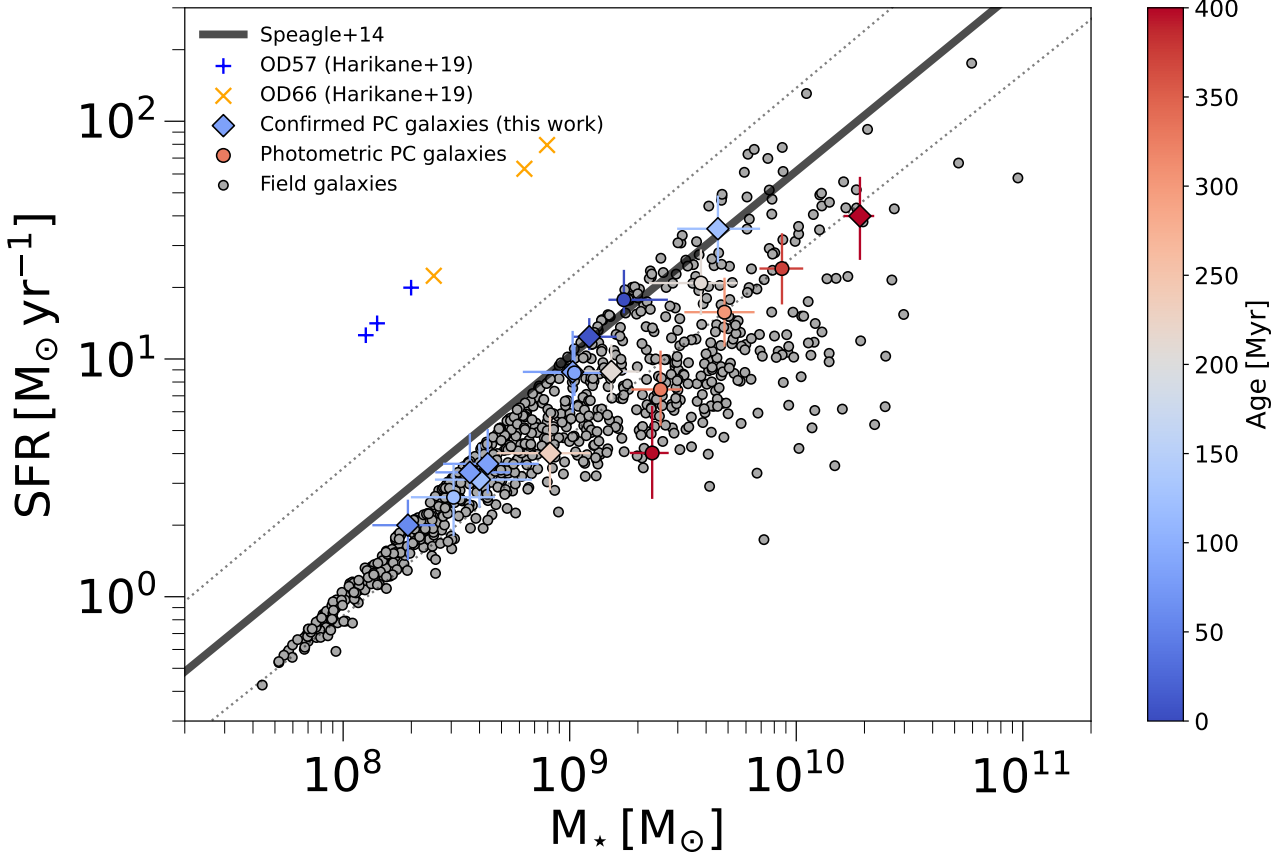


Figure 7. The $SFR - M_*$ plane as derived from BAGPIPES (§4.3.1) for all $z_{\text{phot}} = 5.97 \pm 0.15$ galaxies in COSMOS2020 (grey circles) and for the protocluster galaxies with squares for galaxies with spec-z (grade A & B) and circles for galaxies with photo-z (grade C & D) that were part of the original sample of 19 galaxies from Brinch et al. (2023), both coloured according to their age from BAGPIPES. The galaxy main sequence of Speagle et al. (2014) at $z \simeq 6$ is plotted as a grey line, with the dotted lines on both sides being the 1σ uncertainty. For comparison, the $z = 5.7$ and $z = 6.6$ spectroscopically confirmed LAE-overdensities reported by (Harikane et al. 2019) are also shown (shown as blue + and yellow \times symbols, respectively).

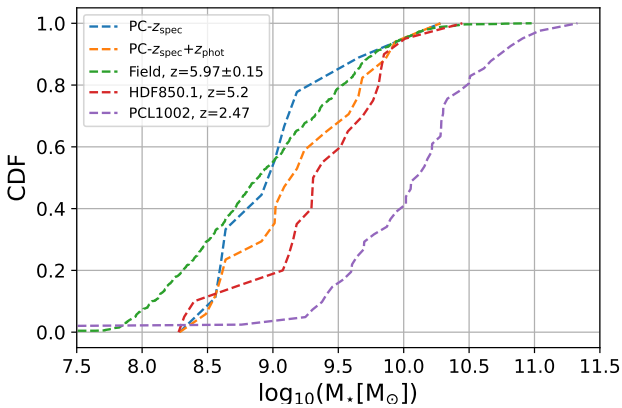


Figure 8. The stellar mass cumulative distribution function (CDF) of the spec-z confirmed galaxies (blue line), the spec-z+photo-z includes 8 galaxies with photo-z from our original 19 galaxy sample (orange line) and of the field (green line) consisting of 876 galaxies at $z_{\text{phot}} = 5.97 \pm 0.15$. For comparison, we also show the stellar mass CDF from the spectroscopically verified protoclusters HDF850.1 at $z = 5.2$ (Calvi et al. 2021) (red line) and PCL1002 at $z = 2.47$ (Casey et al. 2015) (purple line).

4.3.2 The $SFR - M_*$ plane

Figure 7 shows the location of all the galaxies in the $z_{\text{phot}} = 5.97 \pm 0.15$ bin based on the results from the BAGPIPES fitting in the previous section. We confirm the result found in Brinch et al. (2023) that the bulk of the galaxies at $z \sim 6$ appear to be main sequence galaxies. We observe that the $SFR - M_*$ appear to be separated into two populations. A very young, star-forming population and an older, less star-forming population. The very young ages of some galaxies can be explained by the presence of a recent star formation burst. We also observe a tight relation for the main sequence for these young galaxies especially around a stellar mass of $10^8 M_\odot$, which we believe is due to limitations of the templates used by the BAGPIPES modeling⁴. We find that the galaxies in PCz6.05-1 (diamonds and circles) fall on this upper part of the main sequence, with some notable exceptions. The galaxy with the highest mass (ID 582186) has a stellar mass of $10^{10.3} M_\odot$ and an age of 386 Myr, making it the oldest galaxy in our spec-z sample. It is possible that this galaxy is the progenitor of the brightest central cluster galaxies (BCG) that we find at the centres of galaxy clusters at lower redshifts, given its evolved nature and substantial mass at $z = 6$. This is suggestive

⁴ Note that this is not due to the choice of star formation history, as other models were tried and gave an even tighter relationship at low stellar masses.

of downsizing being at play, where, on average, the central BCGs of the most massive (proto)clusters assemble at earlier epochs than those in less massive counterparts (Rennehan et al. 2020). BCGs are formed in high galaxy density protocluster cores, which fits with 582186 being the most massive galaxy in our sample with a central position in the protocluster. One difference between this proto-BCG and the lower- z cluster BCGs is its star formation. 582186 does not appear to be quiescent or off the main sequence, though this is to be expected, as the galaxy is still in its star-forming phase and the difference between it (and protocluster galaxies in general) and the field galaxies is less severe at high- z . Another galaxy not highlighted due to being a C-grade detection in Figure 7 is 392109, with a stellar mass of $10^{9.9} M_{\odot}$ and an SFR of $1.7 M_{\odot}/\text{yr}$ ($\log \text{sSFR} = -9.6$ dex), the galaxy appears to be below the main sequence and could be classified as quiescent. Further study would allow us to investigate the causes behind the quenching. Is the galaxy being quenched due to its environment already at $z = 6$? or is it internal processes in the galaxy that suppress its star formation?

The Harikane et al. (2019) galaxies selected as narrowband LAEs appear to be ~ 1 dex above our main sequence, but we appear to have more massive galaxies in our structure, with about half of the protocluster galaxies being more massive than any of the ones found in OD57 or OD66. The difference is less severe compared to our findings in Brinch et al. (2023) since our protocluster galaxies have generally gotten lower masses when fitting with BAGPIPES than with LEPHARE.

BAGPIPES also allows for the dust obscuration to be estimated in the form of the A_V value. The 10 protocluster galaxies have A_V values in the range $0.04 - 1.11$ with a median of 0.32 . None of the galaxies appear to be heavily dust-obscured, which fits with our expectations from (Brinch et al. 2023) where we saw no strong detection in the available mid- to far-IR data such as MIPS at $24 \mu\text{m}$ and SCUBA-2 at $850 \mu\text{m}$ and ALMA (Ferrara et al. 2022). Since we expect some galaxies to have recently had a starburst due to their young ages from BAGPIPES and their SFH as seen in Appendix ??, we would also expect great amounts of dust to be produced. It is clear that further study is necessary to understand the dust production in these high- z galaxies.

4.4 Stellar mass function and dark matter halo mass

To investigate the distribution of stellar masses in PCz:6.05-1, we show the stellar mass cumulative distribution function (CDF) in Figure 8. For comparison, we also show the CDFs for the protoclusters HDF850.1 (Calvi et al. 2021) and PCL1002 (Casey et al. 2015). We see that the spec- z sample follows the field distribution, being skewed slightly towards higher masses below 9.0 dex and slightly towards lower masses above 9.0 dex, compared to the field. Adding the remaining galaxies with non-detections in our 19 galaxy sample that is within the redshift bin (8 galaxies) the CDF is skewed towards higher masses up until 9.8 dex, where it aligns with the field. This is similar to what we found for this protocluster in Brinch et al. (2023).

With the spectroscopic redshifts and the updated stellar masses, we are able to update our estimate of the dark matter halo mass. For simplicity, we choose the (Behroozi et al. 2013) abundance matching method to estimate the halo mass. For a discussion of other possible ways to estimate the halo mass, we refer the reader to §4.3 in (Brinch et al. 2023). We take the most massive galaxy in our sample, 582186 with a stellar mass of $10^{10.27} M_{\odot}$, and estimate the dark matter halo mass using a stellar mass to halo mass

relationship. We estimate a halo mass of $10^{12.10^{+0.20}_{-0.16}} M_{\odot}$. Following the dark matter halo mass evolution curves of (Chiang et al. 2013), this would suggest that the protocluster would evolve into a Virgo- ($\sim 10^{14} M_{\odot}$) or Coma-like ($\sim 10^{15} M_{\odot}$) cluster in the present day. With the spectroscopic redshift confirmation of multiple galaxies in close proximity and in conjunction with an overall overdense structure that the protocluster lies in as seen in Figure 6, we argue this is likely to be the case. The protocluster position in a large-scale structure allows the protocluster to be fed galaxies away from the central core over time, which will allow it to grow in mass.

To compare with other (proto-)clusters from the literature (Miller et al. 2018; Brinch et al. 2023), we have shown their dark matter halo mass, total stellar mass and richness (i.e. the number of spectroscopically confirmed galaxies in the protocluster) in Figure 9. We see from Figure 9a that our protocluster occupies the ‘cold streams in hot media’ regime where halo-penetrating cold gas flows can help sustain galaxy growth. We also see that our dark matter halo mass estimate is similar to what is found in HDF850.1 (Calvi et al. 2021) and both are in line with the dark matter halo mass evolution track from (Chiang et al. 2013). Figure 9b shows the total stellar mass with redshift, and we see that our protocluster falls within the expected scatter of our protocluster sample and is again close to HDF850.1 at $\sim 10^{11} M_{\odot}$. Figure 9c shows the richness of protoclusters with the total stellar mass, and we see that our protocluster falls in the middle at 10 galaxies for protocluster at $z > 5$.

4.5 Protocluster size and evolution scenarios

If we consider the 8 galaxies within the 4σ contour to be the centre of the protocluster, they cover a $\sim 5.8 \times 5.9 \text{ cMpc}$ area, in line with what is expected from a protocluster at $z = 6$ (Chiang et al. 2013; Chiang et al. 2017; Lovell et al. 2018). The structure is extended more in the z direction, with a distance of 96 cMpc between the lowest and highest redshift galaxy. The reason for this length can be explained by multiple different factors. Firstly is the negative uncertainty due to the nature of the skewed Lyman- α line means that the galaxies could be closer together. Without knowing the Lyman- α escape fraction and being able to model the line before it was attenuated, it is difficult to access where the true line centre is. Secondly is the possibility of the presence of substructures in the protocluster, one above $z = 6$ and one below as seen in figure 10. Considering the eight 4σ galaxies, the distance between the 4 galaxies above $z = 6$ is 18.9 cMpc , while those below $z = 6$ have a distance of 39.0 cMpc . Thirdly, and perhaps most interestingly, is the scenario that this could be two separate protoclusters, which could eventually merge over time. The most massive galaxy below $z = 6$ would have a halo mass of $10^{11.40^{+0.07}_{-0.08}}$. If we consider the two groups of galaxies as separate we can calculate their overdensity by making smaller redshift bins. For the galaxies at $z < 6$ we use a bin of $z = 5.90 \pm 0.05$ and find that 4 of the galaxies with spec- z occupy a 4σ overdensity with a peak of $\delta = 8.2$ (5.7σ). If the procedure is repeated with the $z > 6$ galaxies using a $z = 6.06 \pm 0.05$ bin, we find that 6 of the galaxies with spec- z in the bin occupy a 4σ overdensity with a peak of $\delta = 16.7$ (12.8σ). The overdensity maps for both bins are shown in figure 11. We also note the presence of the second protocluster hitherto reported on is present in both bins. We know for any protocluster dark matter halo to grow to become a cluster in the present day, it must merge with other halos. This is how dark matter halo evolution is tracked in simulation, though a cluster merger tree (see Chiang et al. 2013). If

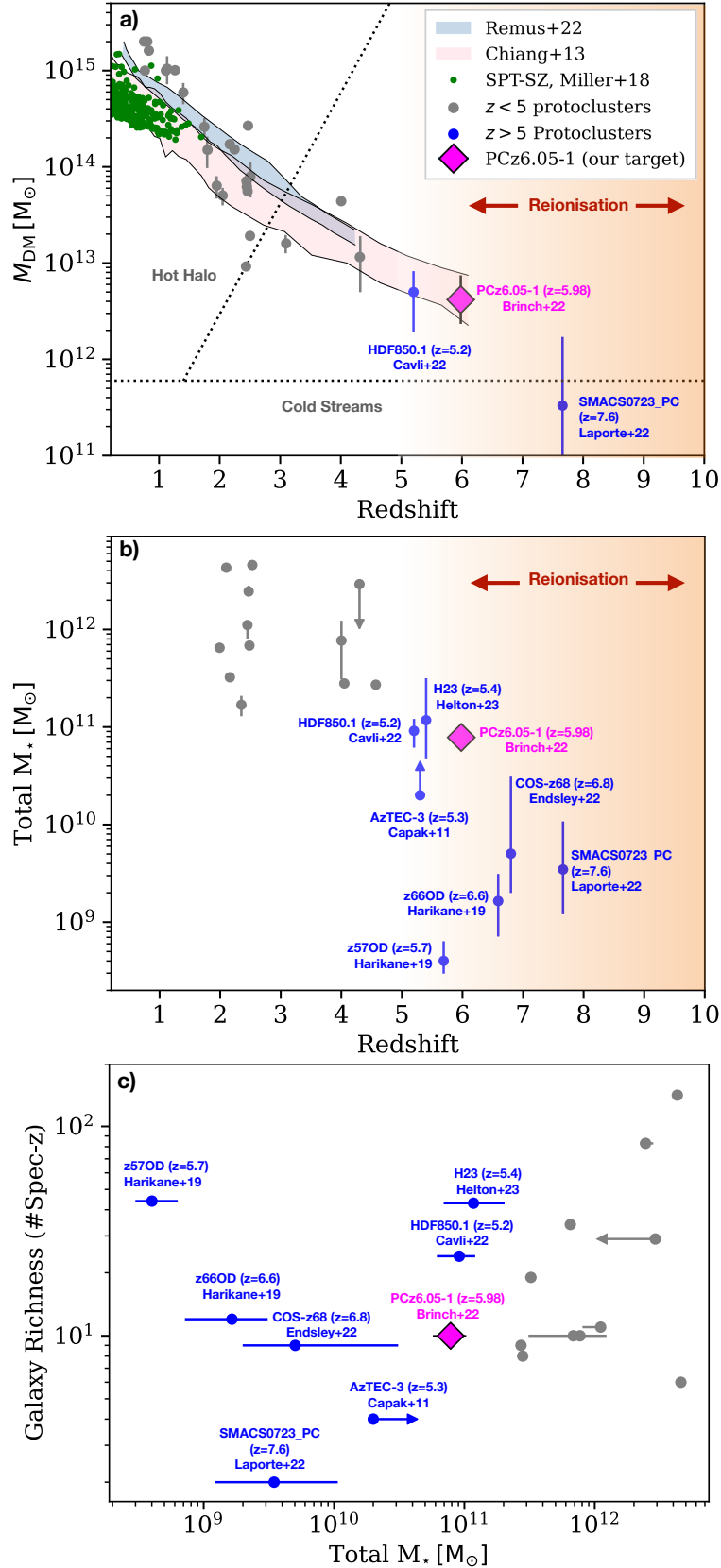


Figure 9. PCz6.05-1 (magenta diamond), is the most massive, and one of the richest, spectroscopically confirmed protoclusters at $z \geq 6$, and has far better OIR multi-wavelength data than other protoclusters at this epoch. **a)** Dark matter halo mass estimates for spectroscopically confirmed protoclusters (compiled from Miller et al. 2018; Brinch et al. 2023) and simulations (Chiang et al. 2013; Remus et al. 2022) across cosmic time. The dashed lines mark different regions of gas inflow and cooling mechanisms on massive halos (Dekel et al. 2013). In the ‘cold streams in hot media’ regime, where PCz6.05-1 is located, halo-penetrating cold gas flows can help sustain galaxy growth. **b)** Same as a) but for the total stellar mass of the protoclusters. **c)** Galaxy richness, defined by the number of spectroscopically confirmed cluster-member galaxies, vs the total stellar mass of protocluster.

this third scenario is true, we are witnessing a snapshot of the growth of protoclusters into becoming the massive galaxy-rich clusters of today.

5 CONCLUSIONS

Using the *DEIMOS* spectrograph on the *Keck* telescope, we have detected the redshifted Lyman- α line toward 10 protocluster galaxies at $z \simeq 6$ identified in the COSMOS field (Brinch et al. 2023). This unequivocally confirms the discovery of a massive and rich protocluster at this early epoch. We obtained an overall spectroscopic success rate of 47% when considering the full sample.

We applied skewed Gaussian fits to the spectral lines and determined their fluxes, equivalent widths and skewness values. Notably, the galaxies exhibited relatively faint line emission, characterized by narrow to intermediate equivalent widths and positive skewness. Additionally, we observed possible continuum detections in two galaxies within our sample, suggesting we have not reached the necessary depth to fully uncover the complete line profiles in these galaxies.

Incorporating the new spectroscopic redshifts into our overdensity analysis, we found a notable increase in the peak overdensity for the protocluster, now measuring $\delta = 11.6$ (10.9σ).

We find that the protocluster is part of a large-scale structure in the centre of the COSMOS field, with multiple significant overdensity peaks connected by filaments. We also report the discovery of a hitherto unknown $z \simeq 6$ protocluster that is part of the same large-scale structure as PCz6.05-1.

We fitted the SEDs of the galaxies using BAGPIPES and found them to be dust-poor main sequence galaxies, in some cases with young ages ($\lesssim 100$ Myr), indicative of a recent starburst. The most massive galaxy (ID 582186) also has the oldest age of 386 Myr and is possibly the progenitor of what will become the brightest cluster galaxy (BCG) at later times.

We estimated the dark matter halo mass and found it to be $\sim 10^{12} M_{\odot}$. This suggests an evolution into a cluster resembling the Virgo or Coma clusters in the present-day Universe.

We discuss the redshift extent of the galaxies' possible evolution scenarios, ranging from possible substructure in the protocluster to the possibility that the galaxies inhabit two separate protocluster that could merge over time.

6 ACKNOWLEDGEMENTS

The Cosmic Dawn Center (DAWN) is funded by the Danish National Research Foundation under grant No. 140. T.R.G. and M.B. are grateful for support from the Carlsberg Foundation via grant No. CF20-0534. The data presented herein were obtained at the W. M. Keck Observatory, which is operated as a scientific partnership among the California Institute of Technology, the University of California and the National Aeronautics and Space Administration. The Observatory was made possible by the generous financial support of the W. M. Keck Foundation. The authors wish to recognize and acknowledge the very significant cultural role and reverence that the summit of Maunakea has always had within the indigenous Hawaiian community. We are most fortunate to have the opportunity to conduct observations from this mountain. This work was partially supported by DeiC National HPC (g.a. DeiC-DTU-L-20210103) and by the "dtu_00026" project.

DATA AVAILABILITY

The original sample of galaxies came from the COSMOS2020 catalogue (Weaver et al. 2022) and is available from <https://cosmos2020.calet.org/>. The original spectra are available upon reasonable request.

REFERENCES

- Behroozi P. S., Wechsler R. H., Conroy C., 2013, *ApJ*, 770, 57
 Brinch M., et al., 2023, *ApJ*, 943, 153
 Calvi R., et al., 2019, *MNRAS*, 489, 3294
 Calvi R., Dannerbauer H., Arrabal Haro P., Rodríguez Espinosa J. M., Muñoz-Tuñón C., Pérez González P. G., Geier S., 2021, *MNRAS*, 502, 4558
 Calzetti D., Armus L., Bohlin R. C., Kinney A. L., Koornneef J., Storchi-Bergmann T., 2000, *ApJS*, 533, 682
 Carnall A. C., McLure R. J., Dunlop J. S., Davé R., 2018, *MNRAS*, 480, 4379
 Casey C. M., et al., 2015, *ApJ*, 808, L33
 Casey C. M., et al., 2019, *ApJ*, 887, 55
 Casey C. M., et al., 2022, *arXiv e-prints*, p. arXiv:2211.07865
 Chabrier G., 2003, *Publications of the Astronomical Society of the Pacific*, 115, 763
 Chanchaiworawit K., et al., 2019, *ApJ*, 877, 51
 Chiang Y.-K., Overzier R., Gebhardt K., 2013, *ApJ*, 779, 127
 Chiang Y.-K., Overzier R. A., Gebhardt K., Henriques B., 2017, *ApJ*, 844, L23
 Childs H. J. T., Stanway E. R., 2018, *MNRAS*, 480, 1938
 Cooper M. C., et al., 2008, *MNRAS*, 383, 1058
 Dekel A., Zolotov A., Tweed D., Cacciato M., Ceverino D., Primack J. R., 2013, *MNRAS*, 435, 999
 Elbaz D., et al., 2007, *A&A*, 468, 33
 Endsley R., Stark D. P., 2022, *MNRAS*, 511, 6042
 Endsley R., Stark D. P., Whittler L., Topping M. W., Chen Z., Plat A., Chisholm J., Charlot S., 2023, *MNRAS*, 524, 2312
 Faber S. M., et al., 2003, in Iye M., Moorwood A. F. M., eds, *Society of Photo-Optical Instrumentation Engineers (SPIE) Conference Series Vol. 4841, Instrument Design and Performance for Optical/Infrared Ground-based Telescopes*. pp 1657–1669, doi:10.1117/12.460346
 Ferland G. J., et al., 2013, *Rev. Mex. Astron. Astrofis.*, 49, 137
 Ferland G. J., et al., 2017, *Rev. Mex. Astron. Astrofis.*, 53, 385
 Ferrara A., et al., 2022, *Monthly Notices of the Royal Astronomical Society*, 512, 58
 Guita L., et al., 2015, *A&A*, 576, A51
 Harikane Y., et al., 2019, *ApJ*, 883, 142
 Hasinger G., et al., 2018, *ApJ*, 858, 77
 Helton J. M., et al., 2023, *arXiv e-prints*, p. arXiv:2302.10217
 Hu W., et al., 2021, *Nature Astronomy*,
 Ilbert O., et al., 2006, *A&A*, 457, 841
 Jin S., et al., 2019, *ApJ*, 887, 144
 Kerutt J., et al., 2022, *A&A*, 659, A183
 Khostovan A. A., Kartaltepe J., Ilbert O., Salvato M., Casey C., 2023, In prep.
 Kodama T., Smail I., Nakata F., Okamura S., Bower R. G., 2001, *ApJ*, 562, L9
 Kroese D. P., Rubinstejn R. Y., 2011, *WIREsComput.Stat*, 4, 48
 Laporte N., Zitrin A., Dole H., Roberts-Borsani G., Furtak L. J., Witten C., 2022, *A&A*, 667, L3
 Leja J., Carnall A. C., Johnson B. D., Conroy C., Speagle J. S., 2019, *ApJ*, 876, 3
 Long A. S., et al., 2020, *ApJ*, 898, 133
 Lovell C. C., Thomas P. A., Wilkins S. M., 2018, *MNRAS*, 474, 4612
 Lovell C. C., Vijayan A. P., Thomas P. A., Wilkins S. M., Barnes D. J., Irodoutou D., Roper W., 2021, *MNRAS*, 500, 2127
 Mallery R. P., et al., 2012, *ApJ*, 760, L28
 Mason C. A., Gronke M., 2020, *MNRAS*, 499, 1395
 Miller T. B., et al., 2018, *Nature*, 556, 469

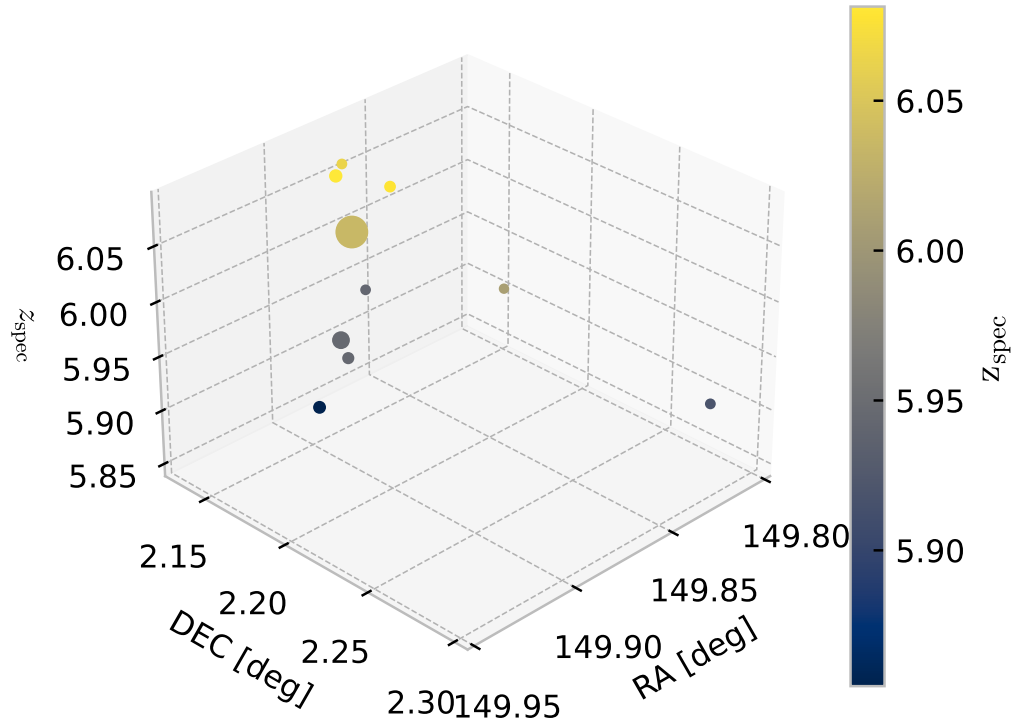


Figure 10. 3D distribution of galaxies with spectroscopic redshift in RA, DEC, redshift. points with larger sizes have larger stellar masses and are coloured according to their spectroscopic redshift.

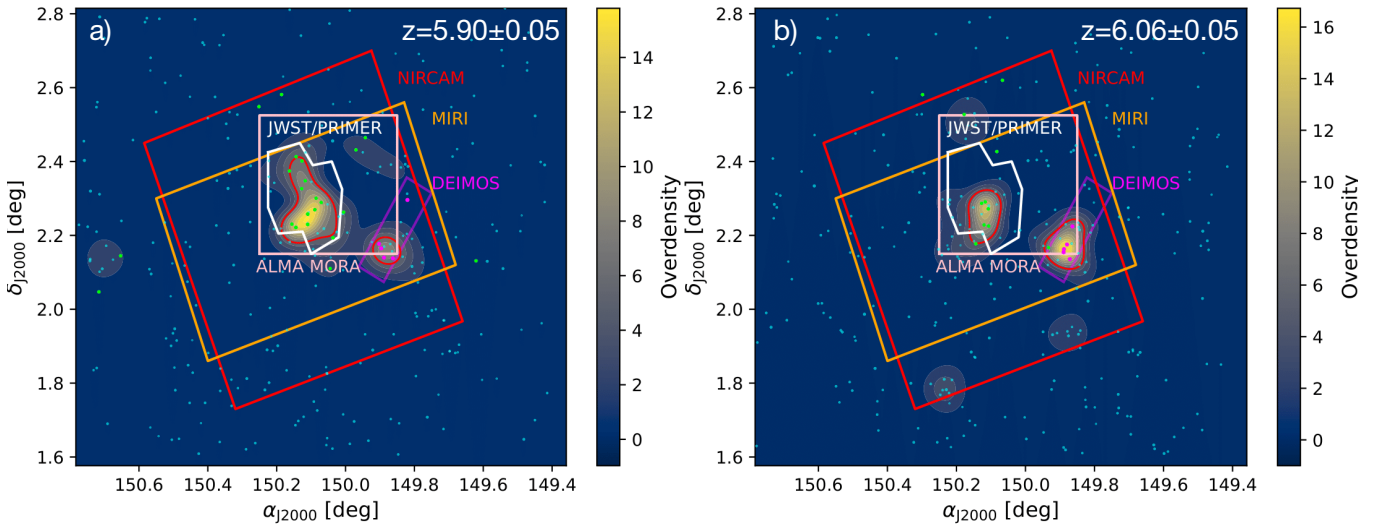


Figure 11. Galaxy overdensity maps using a) $z = 5.90 \pm 0.05$ bin and b) $z = 6.06 \pm 0.05$ bin. The setup is the same as figure 6.

Table 3. List of all confirmed Ly α detections with their parameters; Columns: (1) COSMOS2020 catalogue ID.; (2) & (3) R.A. and Dec.; (4) spectroscopic redshift; (5) spectroscopically measured Ly α flux; (6) spectroscopically measured Ly α luminosity; (7) Skewness (gamma parameter), galaxies without have a double-peaked Ly α profile; (8) detection grade: A = secured detection, B = sound detection, C = marginal detection and D=non-detection. The numbers in the parenthesis show the criteria fulfilled.

ID	RA <i>hh:mm:ss.ss</i>	Dec <i>dd:mm:ss.ss</i>	z_{spec}	$F_{\text{Ly}\alpha, \text{spec}}$ [$10^{-18} \text{erg s}^{-1} \text{cm}^{-2}$]	$L_{\text{Ly}\alpha, \text{spec}}$ [$10^{42} \text{erg s}^{-1}$]	Skewness [γ]	Grade
(1)	(2)	(3)	(4)	(5)	(6)	(7)	(8)
Protocluster members							
70505	09:59:16.86	02:17:45.20	5.9191 ^{+0.0003} _{-0.0003}	5.21 ^{+0.19} _{-0.17}	2.014 ^{+0.974} _{-0.067}	2.87 ^{+0.43} _{-0.53}	B(1,2)
156780	09:59:29.14	02:08:08.38	6.0642 ^{+0.0003} _{-0.0003}	1.92 ^{+0.22} _{-0.24}	0.785 ^{+0.088} _{-0.097}	6.10 ^{+4.19} _{-2.62}	B(1,2)
186512	09:59:27.01	02:08:17.01	5.9240 ^{+0.0001} _{-0.0001}	6.79 ^{+0.25} _{-0.25}	2.628 ^{+0.098} _{-0.098}	10.77 ^{+4.00} _{-1.54}	B(1,2)
220530	09:59:27.36	02:13:27.56	6.0088 ^{+0.0001} _{-0.0001}	1.28 ^{+0.09} _{-0.10}	0.512 ^{+0.038} _{-0.039}	8.52 ^{+53.26} _{-2.94}	B(1,3)
225263	09:59:33.21	02:08:23.24	5.8547 ^{+0.0002} _{-0.0002}	0.79 ^{+0.07} _{-0.06}	0.296 ^{+0.025} _{-0.022}	23.19 ^{+1675.38} _{-14.73}	A(1,2,3)
361608	09:59:30.58	02:08:57.78	5.9070 ^{+0.0001} _{-0.0010}	0.73 ^{+0.50} _{-0.39}	0.282 ^{+0.192} _{-0.150}	4.87 ^{+29.17} _{-4.74}	C(1)
392109	09:59:21.48	02:14:09.26	6.0090 ^{+0.0004} _{-0.0003}	0.47 ^{+0.05} _{-0.05}	0.189 ^{+0.021} _{-0.020}	6.22 ^{+35.17} _{-4.47}	C(3)
441761	09:59:35.16	02:09:53.31	5.9455 ^{+0.0004} _{-0.0003}	0.63 ^{+0.10} _{-0.08}	0.246 ^{+0.038} _{-0.032}	5.26 ^{+13.37} _{-2.74}	B(1,3)
482804	09:59:33.50	02:09:17.17	6.0814 ^{+0.0017} _{-0.0002}	0.64 ^{+0.08} _{-0.07}	0.265 ^{+0.033} _{-0.030}	9.84 ^{+30.96} _{-1.89}	A(1,2,3)
573604	09:59:36.65	02:10:37.28	5.9440 ^{+0.0002} _{-0.0002}	1.05 ^{+0.08} _{-0.07}	0.409 ^{+0.030} _{-0.029}	23.48 ^{+1209.28} _{-7.83}	A(1,2,3)
582186	09:59:33.25	02:09:45.81	6.0359 ^{+0.0002} _{-0.0001}	1.12 ^{+0.12} _{-0.10}	0.453 ^{+0.048} _{-0.038}	31.75 ^{+1082.30} _{-27.03}	B(1,2)
759747	09:59:31.11	02:10:31.32	6.0781 ^{+0.0004} _{-0.0001}	0.83 ^{+0.07} _{-0.11}	0.341 ^{+0.030} _{-0.046}	3.06 ^{+952.19} _{-3.02}	B(1,2)
Interlopers							
169797	09:59:16.21	02:18:17.85	6.3156 ^{+0.0001} _{-0.0001}	6.62 ^{+0.16} _{-0.15}	2.974 ^{+0.072} _{-0.065}	7.97 ^{+16.99} _{-1.98}	B(1,2)
345111	09:59:35.75	02:09:18.69	4.7571 ^{+0.0015} _{-0.0006}	0.73 ^{+0.08} _{-0.08}	0.169 ^{+0.019} _{-0.020}	1.61 ^{+1.21} _{-1.57}	C(1)
350720	09:59:34.48	02:13:54.03	5.5594 ^{+0.0014} _{-0.0002}	0.62 ^{+1.41} _{-0.11}	0.207 ^{+0.470} _{-0.038}	3.46 ^{+28.84} _{-6.60}	A(1,2,3)
369661	09:59:23.33	02:14:04.42	6.1322 ^{+0.0037} _{-0.0034}	1.96 ^{+1.96} _{-0.25}	0.825 ^{+0.817} _{-0.106}	5.51 ^{+102.56} _{-7.80}	C(2)
444487	09:59:30.56	02:09:10.48	4.2729 ^{+0.0004} _{-0.0004}	5.57 ^{+0.09} _{-0.08}	1.001 ^{+0.017} _{-0.015}	-0.31 ^{+0.31} _{-0.33}	A(1,2,3)
654354	09:59:16.82	02:20:15.24	6.3200 ^{+0.0002} _{-0.0003}	0.57 ^{+0.14} _{-0.13}	0.258 ^{+0.062} _{-0.059}	17.58 ^{+566.68} _{-16.11}	C(1)
958367	09:59:24.54	02:12:27.15	6.1987 ^{+0.0013} _{-0.0005}	0.80 ^{+0.07} _{-0.07}	0.342 ^{+0.029} _{-0.028}	1.45 ^{+1.96} _{-1.36}	B(1,3)
Non-detections							
127337	09:59:22.49	02:12:53.54					D
142959	09:59:20.56	02:13:10.62					D
187778	09:59:23.08	02:13:20.10					D
324132	09:59:31.67	02:13:50.86					D
339126	09:59:06.74	02:18:56.87					D
413243	09:59:23.09	02:09:04.73					D
694706	09:59:38.29	02:11:12.90					D
742465	09:59:35.88	02:11:29.06					D
783817	09:59:27.96	02:10:39.35					D
858263	09:59:26.26	02:16:28.20					D
901963	09:59:44.44	02:07:10.92					D

Newville M., Stensitzki T., Allen D. B., Ingargiola A., 2014, LMFIT: Non-Linear Least-Square Minimization and Curve-Fitting for Python, doi:10.5281/zenodo.11813

Oke J. B., 1974, *ApJS*, 27, 21

Ono Y., et al., 2017, *Publications of the Astronomical Society of Japan*, 70

Overzier R. A., 2016, *A&ARv*, 24, 14

Poggianti B. M., Smail I., Dressler A., Couch W. J., Barger A. J., Butcher H., Ellis R. S., Augustus Oemler J., 1999, *The Astrophysical Journal*, 518, 576

Prochaska J. X., et al., 2020a, pypeit/PypeIt: Release 1.0.0, doi:10.5281/zenodo.3743493

Prochaska J. X., et al., 2020b, *Journal of Open Source Software*, 5, 2308

Remus R.-S., Dolag K., Dannerbauer H., 2022, *arXiv e-prints*, p. arXiv:2208.01053

Rennehan D., Babul A., Hayward C. C., Bottrell C., Hani M. H., Chapman S. C., 2020, *MNRAS*, 493, 4607

Rousselot P., Lidman C., Cuby J. G., Moreels G., Monnet G., 2000, *A&A*, 354, 1134

Scholtz J., et al., 2023, *arXiv e-prints*, p. arXiv:2306.09142

Scoville N., et al., 2013, *ApJS*, 206, 3

Shuntov M., et al., 2022, *A&A*, 664, A61

Speagle J. S., Steinhardt C. L., Capak P. L., Silverman J. D., 2014, *ApJS*, 214, 15

Stanway E. R., Bunker A. J., McMahon R. G., Ellis R. S., Treu T., McCarthy P. J., 2004, *ApJ*, 607, 704

Stark D. P., Ellis R. S., Ouchi M., 2011, *ApJ*, 728, L2

Storey P. J., Zeppen C. J., 2000, *MNRAS*, 312, 813

Tacchella S., et al., 2023, *ApJ*, 952, 74

Tapken C., Appenzeller I., Noll S., Richling S., Heidt J., Meinköhn E., Mehlert D., 2007, *A&A*, 467, 63

Toshikawa J., et al., 2012, *ApJ*, 750, 137

Toshikawa J., et al., 2014, *ApJ*, 792, 15

Weaver J. R., et al., 2022, *ApJS*, 258, 11

Wilkins S. M., et al., 2023, *MNRAS*, 518, 3935

Williams C. C., et al., 2019, *ApJ*, 884, 154

Zabludoff A. I., Zaritsky D., Lin H., Tucker D., Hashimoto Y., Shectman S. A., Oemler A., Kirshner R. P., 1996, *ApJ*, 466, 104

Zavala J. A., 2021, *RNAAS*, 5, 15

Table 4. List of fit parameters for Ly α detections; Columns: (1) name; (2) Baseline from fit (3) lower limit of the Ly α rest-frame equivalent width, followed by the width if continuum is detected, both using values noise/flux 100 Å on the red end of the line.

ID (1)	Baseline [$10^{-18}\text{erg s}^{-1}\text{ cm}^{-2}$] (2)	EW $_{0,\text{Ly}\alpha}$ [Å] (3)
70505	-0.029 ^{+0.002} _{-0.002}	> 16
156780	-0.006 ^{+0.004} _{-0.004}	> 5
169797	0.030 ^{+0.003} _{-0.003}	> 12/18
186512	0.007 ^{+0.003} _{-0.003}	> 11
220530	-0.007 ^{+0.003} _{-0.002}	> 4
225263	0.000 ^{+0.003} _{-0.004}	> 1
345111	-0.015 ^{+0.002} _{-0.002}	> 2
350720	0.022 ^{+0.005} _{-0.005}	> 2
361608	0.000 ^{+0.003} _{-0.004}	> 2
369661	-0.033 ^{+0.004} _{-0.012}	> 4
392109	-0.007 ^{+0.003} _{-0.002}	> 1
441761	0.040 ^{+0.004} _{-0.004}	> 1/3
444487	-0.015 ^{+0.004} _{-0.004}	> 15
482804	0.010 ^{+0.006} _{-0.006}	> 1
573604	0.081 ^{+0.004} _{-0.004}	> 2/1
582186	-0.007 ^{+0.004} _{-0.004}	> 2
654354	-0.001 ^{+0.003} _{-0.002}	> 1
759747	-0.017 ^{+0.005} _{-0.003}	> 2
958367	-0.019 ^{+0.003} _{-0.003}	> 3

APPENDIX A: INTERLOPERS GALAXIES IMAGES AND SPECTRA

Figure A1 show the true color images and spectra for the interloper galaxies.

APPENDIX B: TABLE FOR OTHER OBJECTS ON SLIT

Table B1 shows the lines and redshift found for other objects on the DEIMOS slits.

APPENDIX C: COMPARISON OF STAR FORMATION HISTORIES FOR A CONSTANT OR NON-PARAMETRIC MODEL WHEN USING BAGPIPES

Figure C1 shows the SFH for our 10 protocluster galaxies using a constant SFH model and a non-parametric one when fitting with BAGPIPES.

APPENDIX D: BAGPIPES SED FIT FOR PROTOCLUSTER GALAXIES WITH SPEC-Z

Figure D1 shows the BAGPIPES fit for our 10 protocluster galaxies using a non-parametric SFH.

This paper has been typeset from a $\text{\TeX}/\text{\LaTeX}$ file prepared by the author.

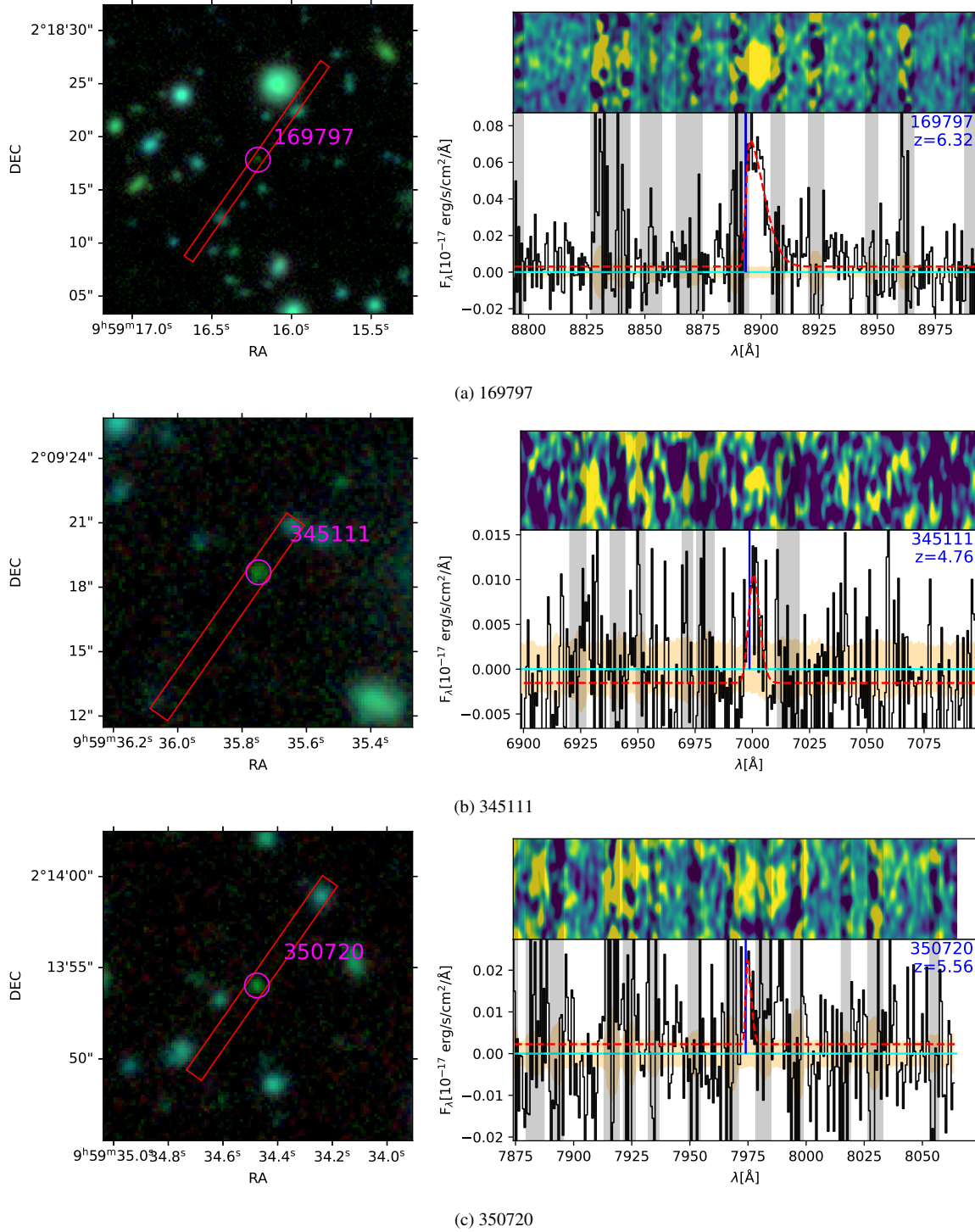
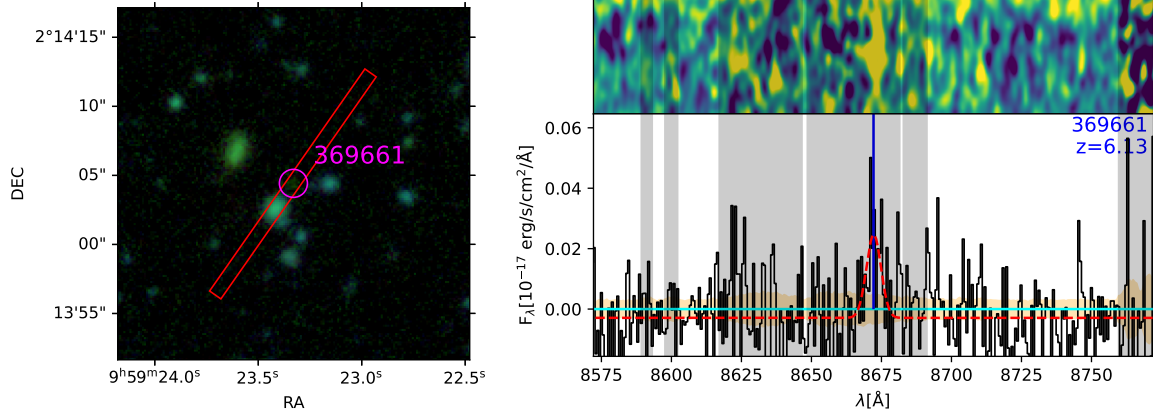
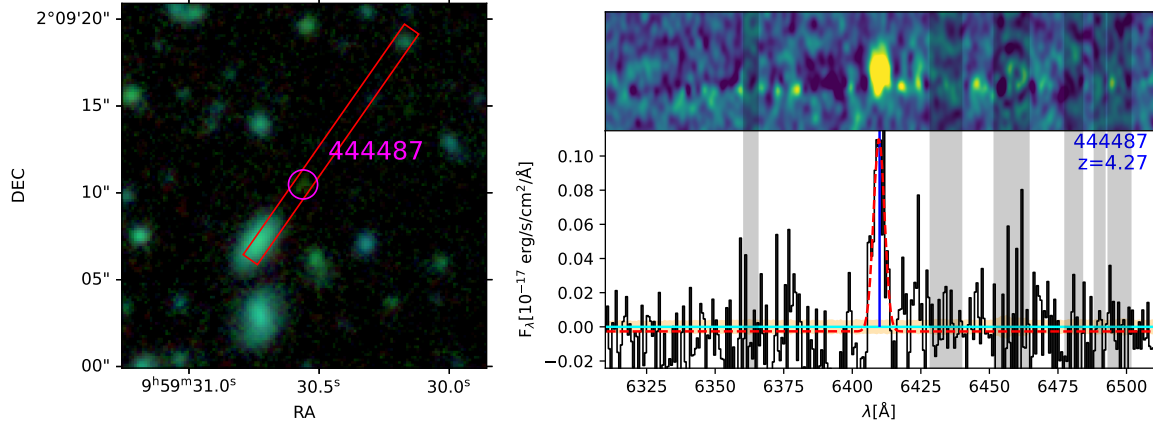


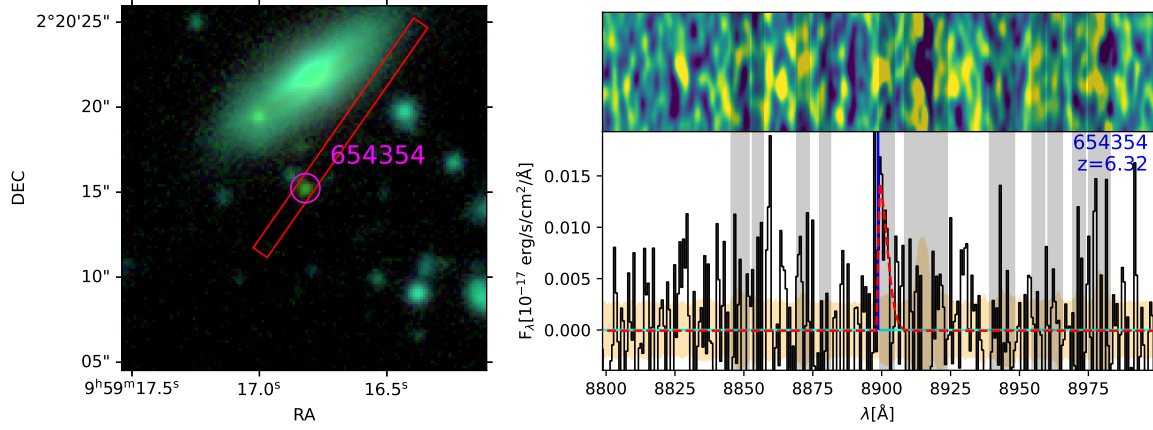
Figure A1. Continued on next page.



(d) 369661

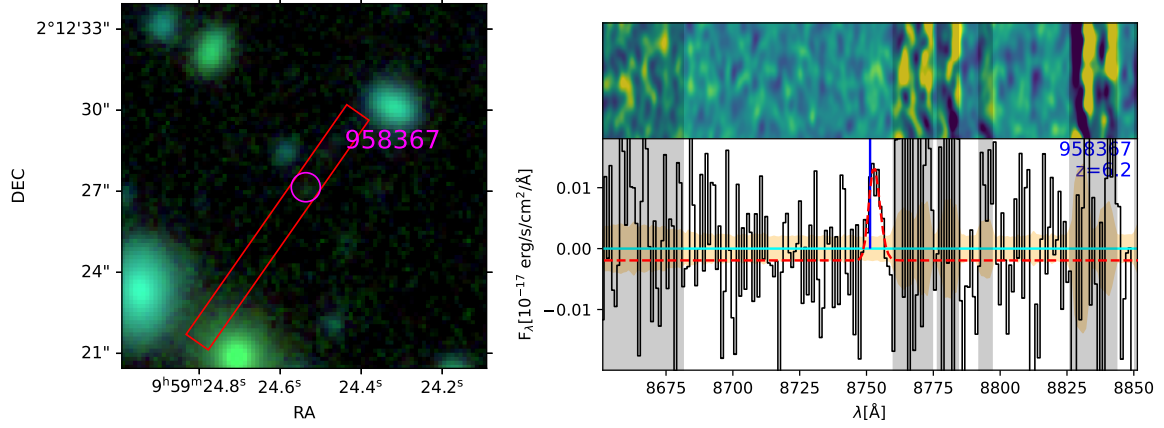


(e) 444487



(f) 654354

Figure A1. Continued on next page.



(g) 958367

Figure A1. 2D, 1D and Yzi RGB true-colour images of the interloper galaxies. The left side shows VISTA Yzi RGB true colour images using the COSMOS2020 catalogue photometry. The slit used to observe each object is plotted on top of the image and a magenta circle with an accompanying object ID is shown to highlight the position of the object in the image. The right side shows three-panel figures of the 2D (top), 1D (middle) and Signal-to-Noise Ratio (SNR) (bottom) for the line detection of each object. A Gaussian filter has been applied to the 2D spectra to visually highlight the detection. The black solid lines are the extracted 1D spectra. The vertical blue line indicated the spectroscopic redshift of the objects. The shaded yellow area is the noise. The grey-shaded regions in all three panels highlight the sky regions, where skylines are prevalent.

Table B1. List of other lines found from other objects present on the slits with their parameters; Columns: (1) COSMOS2020 catalogue ID.; (2) & (3) R.A. and Dec.; (4) spectroscopic redshift. The lines observed are [OII] at 3726 Å and 3729 Å, Hβ at 4861 Å and [OIII] at 4959 Å and 5007 Å.

ID	RA	Dec	z_{spec}
(1)	<i>hh:mm:ss.ss</i> (2)	<i>dd:mm:ss.ss</i> (3)	
Other objects on slit			
159501-[OII]	09:59:16.43	02:18:12.28	$0.8915^{+0.0001}_{-0.0001}$
159501-[OII]3729	09:59:16.43	02:18:12.28	$0.8916^{+0.0001}_{-0.0001}$
159501-Hβ	09:59:16.43	02:18:12.28	$0.8915^{+0.0001}_{-0.0001}$
159501-[OIII]4959	09:59:16.43	02:18:12.28	$0.8910^{+0.0001}_{-0.0001}$
159501-[OIII]5007	09:59:16.43	02:18:12.28	$0.8915^{+0.0001}_{-0.0001}$
169710-[OII]3726	09:59:20.37	02:13:14.01	$1.0276^{+0.0001}_{-0.0001}$
169710-[OII]3729	09:59:20.37	02:13:14.01	$1.0276^{+0.0001}_{-0.0001}$
207402-[OII]3726	09:59:15.96	02:18:22.39	$0.8525^{+0.0001}_{-0.0001}$
207402-[OII]3729	09:59:15.96	02:18:22.39	$0.8525^{+0.0001}_{-0.0001}$
207402-[OIII]4959	09:59:15.96	02:18:22.39	$0.8527^{+0.0003}_{-0.0001}$
207402-[OIII]5007	09:59:15.96	02:18:22.39	$0.8525^{+0.0001}_{-0.0001}$
216791-[OII]3726	09:59:27.42	02:08:16.19	$0.8182^{+0.0001}_{-0.0001}$
216791-[OII]3729	09:59:27.42	02:08:16.19	$0.8181^{+0.0001}_{-0.0001}$
216791-[OIII]4959	09:59:27.42	02:08:16.19	$0.8185^{+0.0001}_{-0.0001}$
216791-[OIII]5007	09:59:27.42	02:08:16.19	$0.8192^{+0.0001}_{-0.0001}$
356445-[OII]3726	09:59:30.17	02:19:03.84	$0.9250^{+0.0001}_{-0.0001}$
356445-[OII]3729	09:59:30.17	02:19:03.84	$0.9243^{+0.0001}_{-0.0001}$
369301-[OII]3726	09:59:23.41	02:14:02.56	$0.9571^{+0.0001}_{-0.0001}$
369301-[OII]3729	09:59:23.41	02:14:02.56	$0.9572^{+0.0001}_{-0.0001}$
407631-Hβ	09:59:30.17	02:19:19.83	$0.3732^{+0.0001}_{-0.0001}$
407631-[OIII]4959	09:59:30.17	02:19:19.83	$0.3733^{+0.0001}_{-0.0001}$
407631-[OIII]5007	09:59:30.17	02:19:19.83	$0.3734^{+0.0001}_{-0.0001}$
437549-[OII]3726	09:59:30.73	02:09:07.20	$1.0367^{+0.0001}_{-0.0001}$
437549-[OII]3729	09:59:30.73	02:09:07.20	$1.0363^{+0.0001}_{-0.0001}$

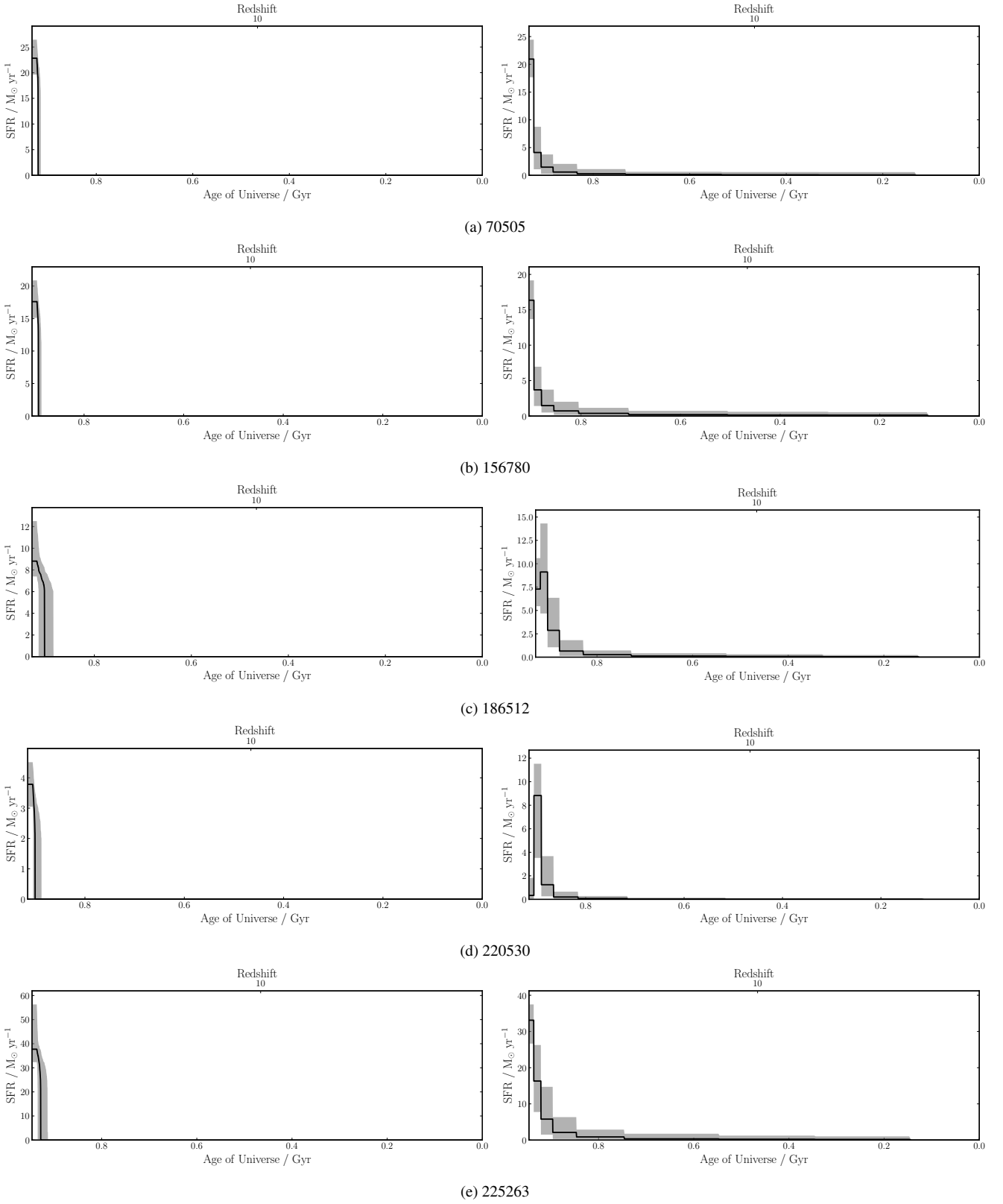


Figure C1. Continued on next page.

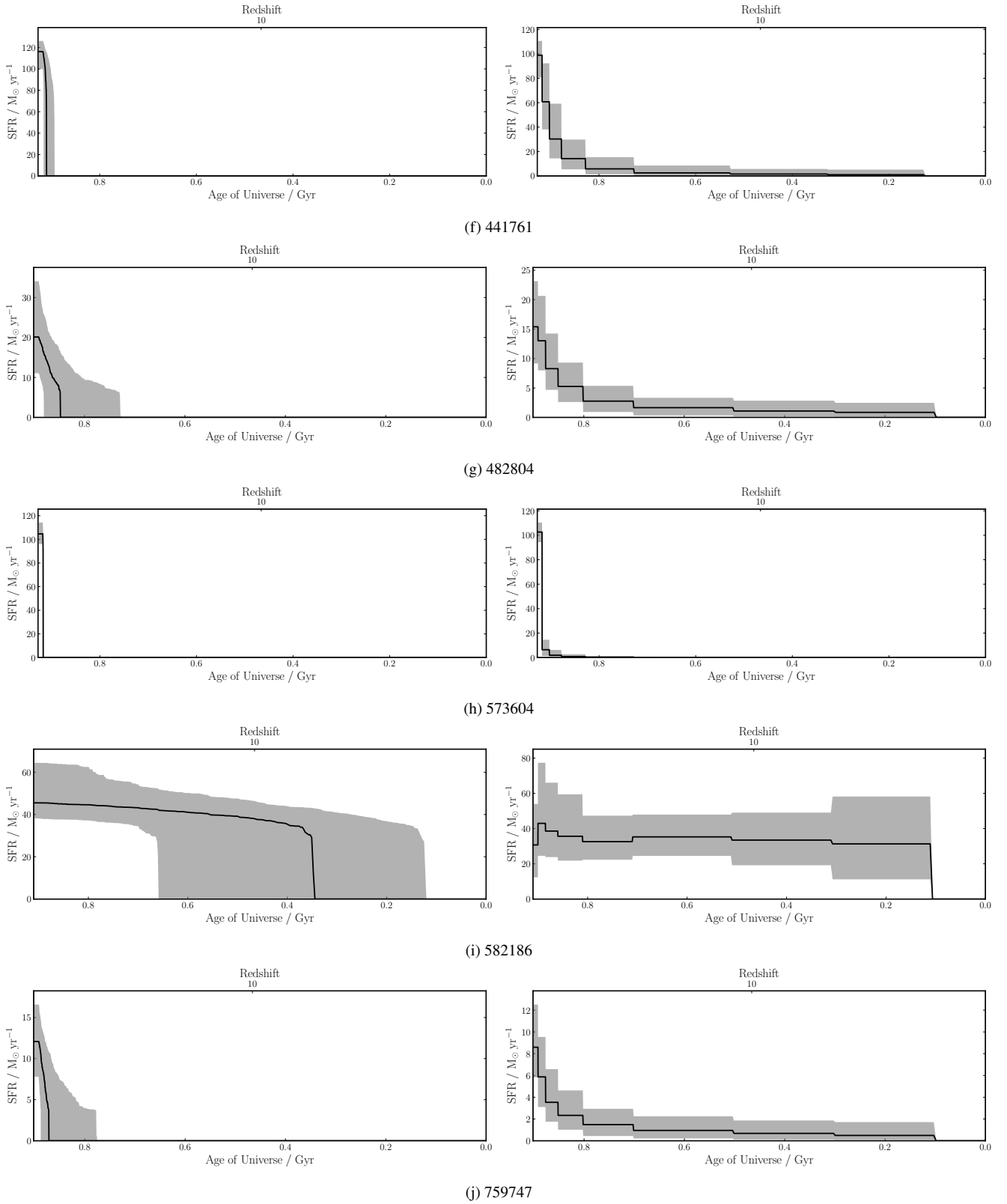


Figure C1. Star formation histories from BAGPIPES fitting to our protocluster galaxies. **(left)** a constant SFH model. **(right)** a non-parametric SFH model.

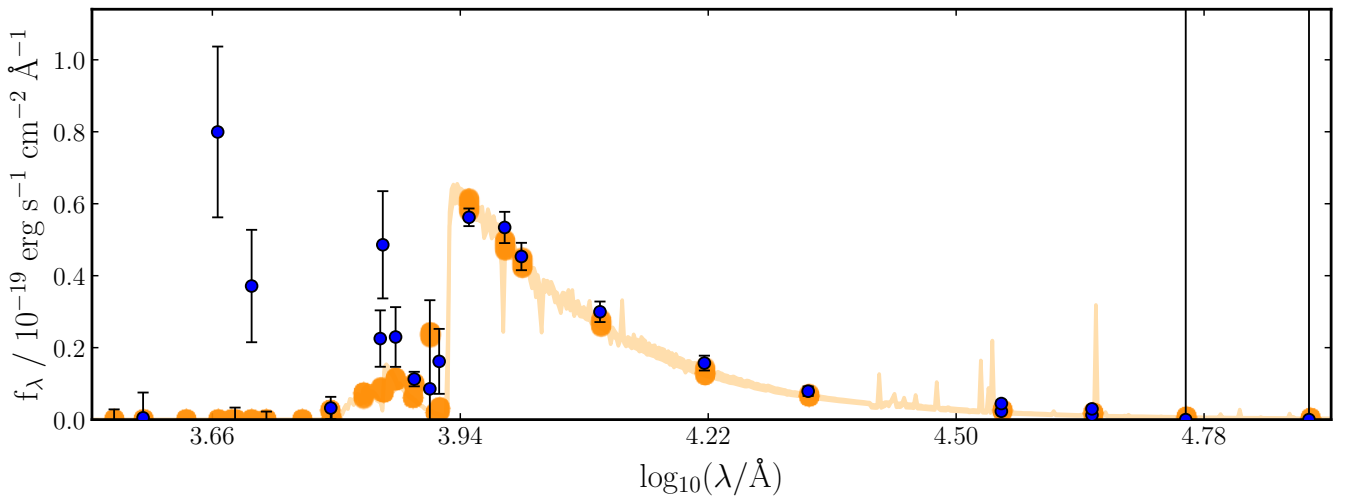
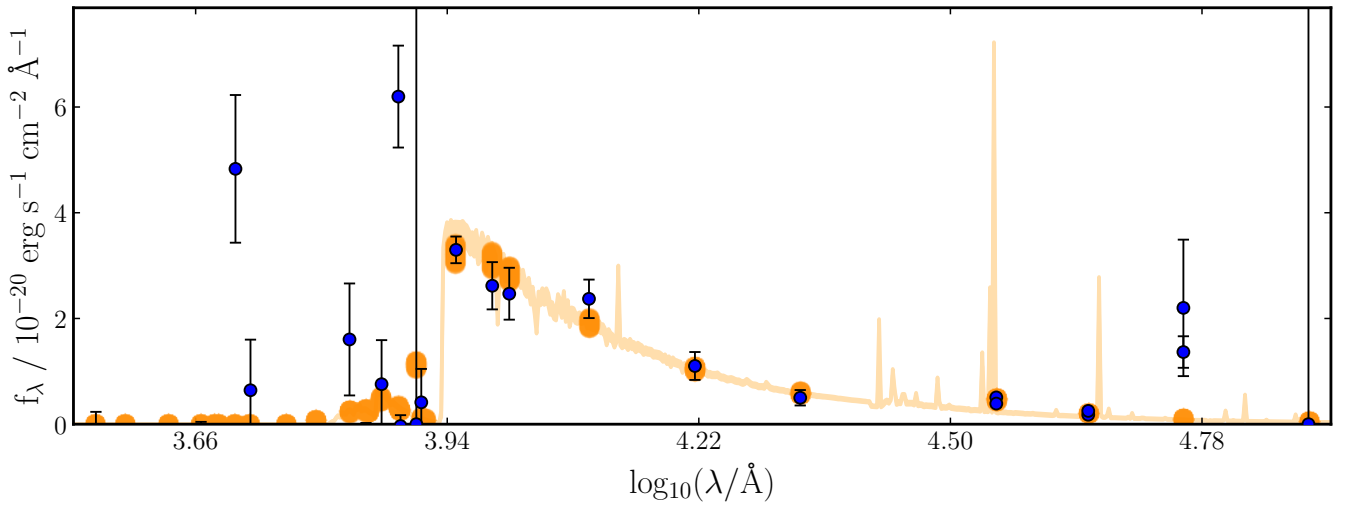
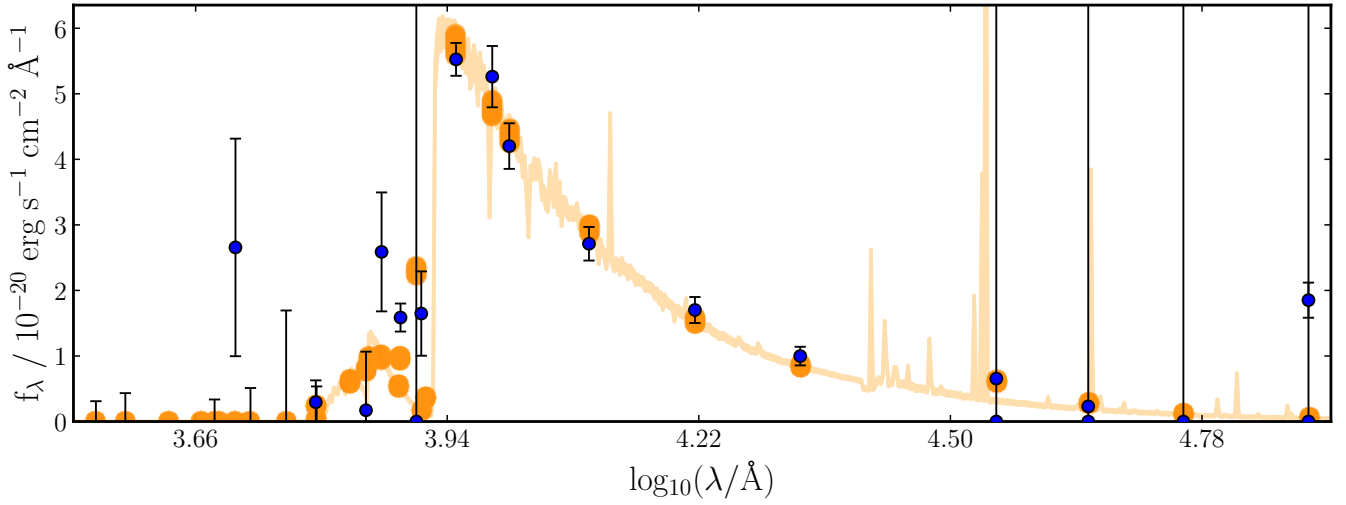


Figure D1. Continued on next page.

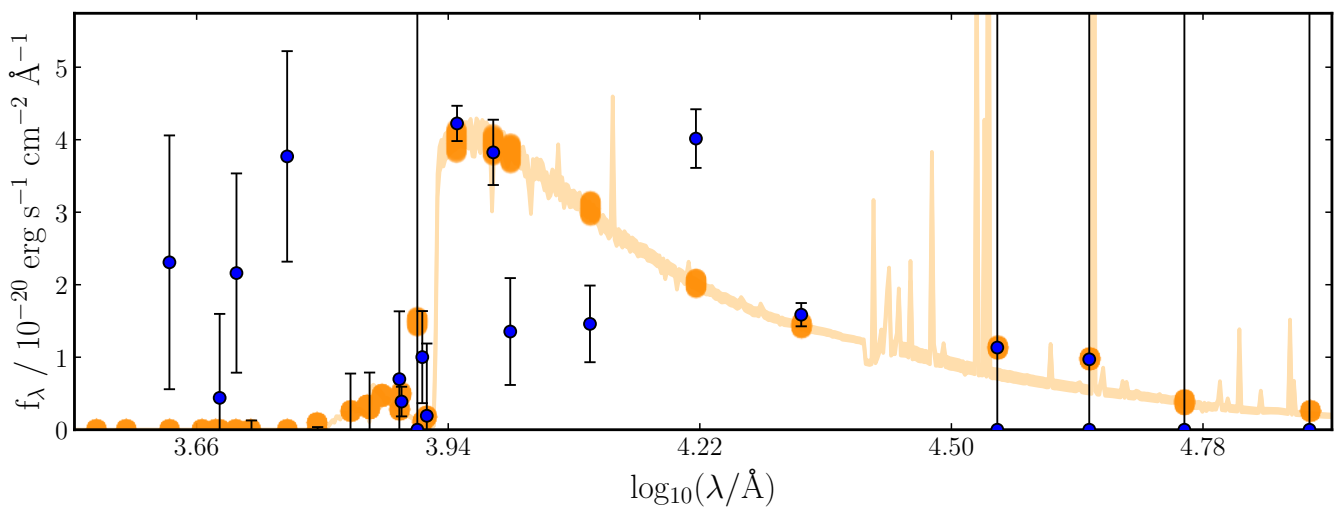
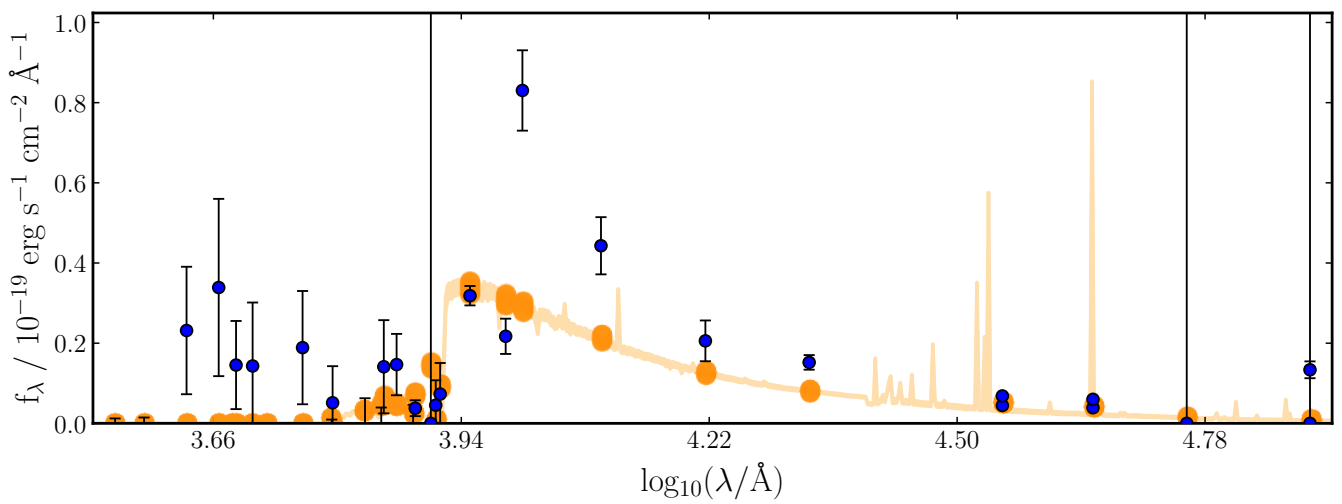
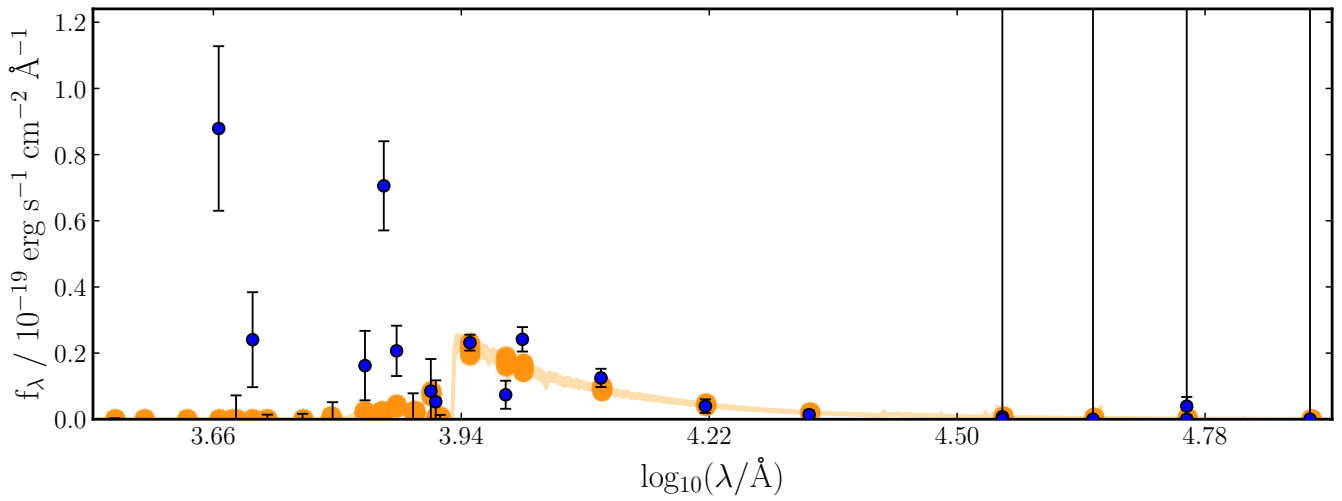
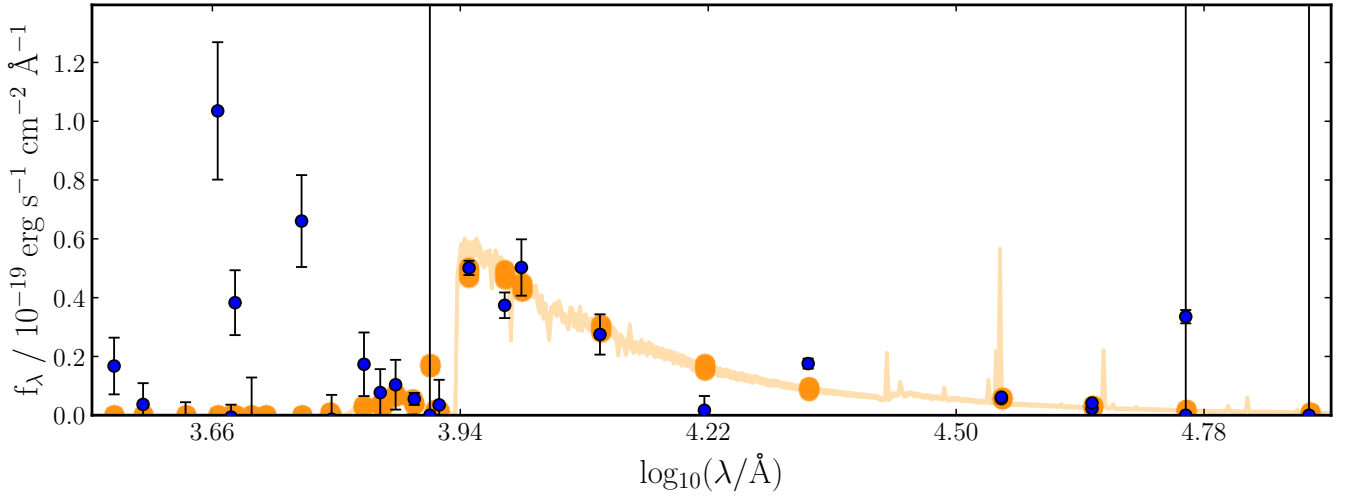
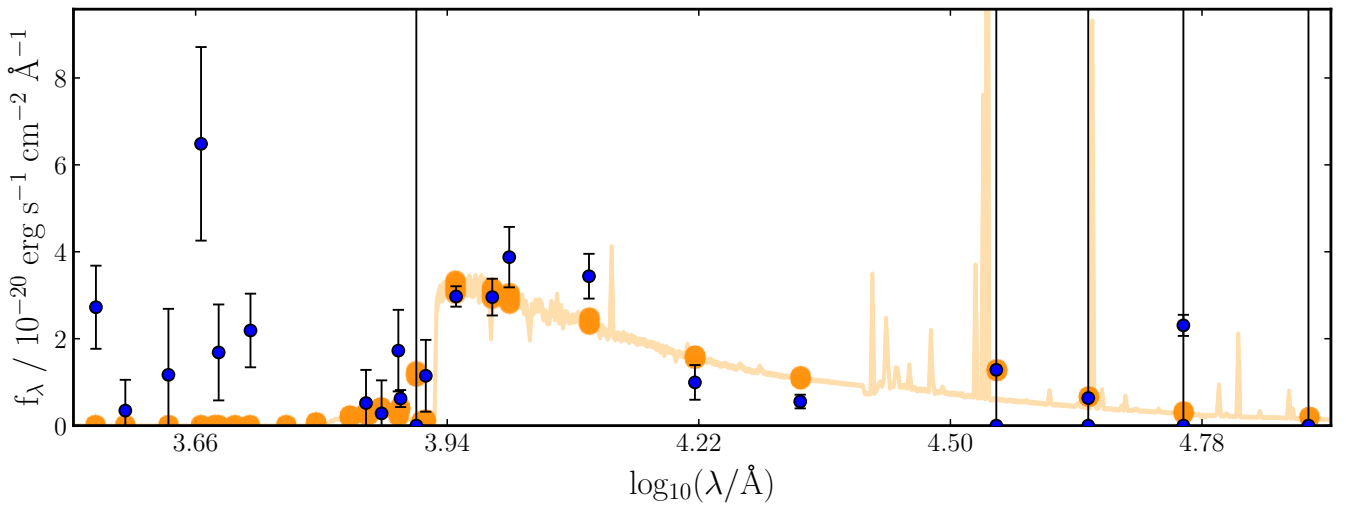


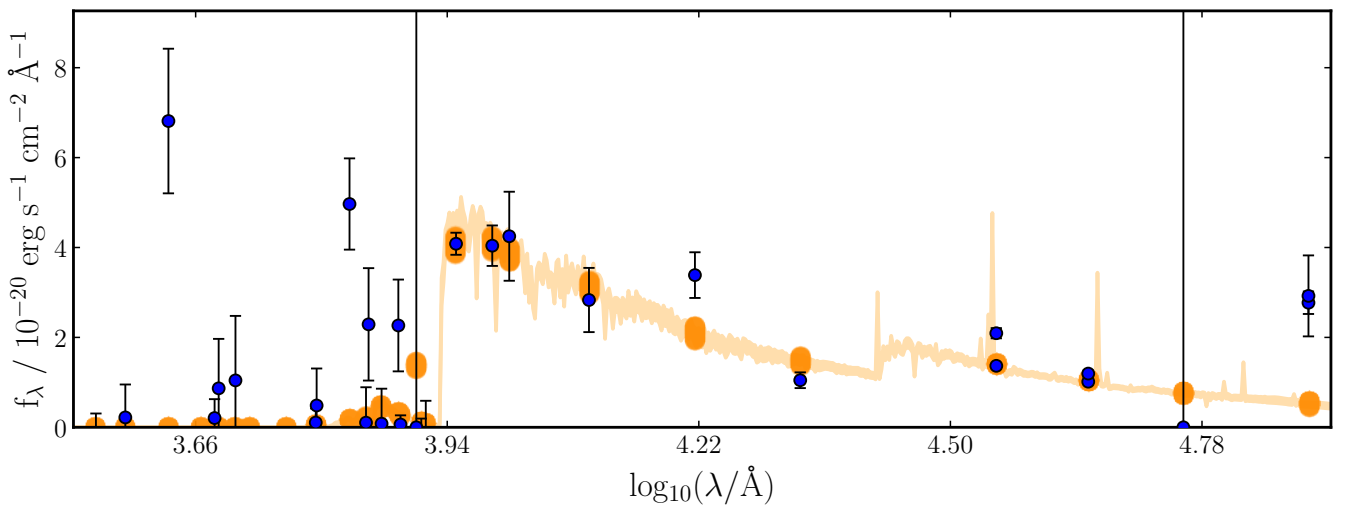
Figure D1. Continued on next page.



(g) 482804



(h) 573604



(i) 582186

Figure D1. Continued on next page.

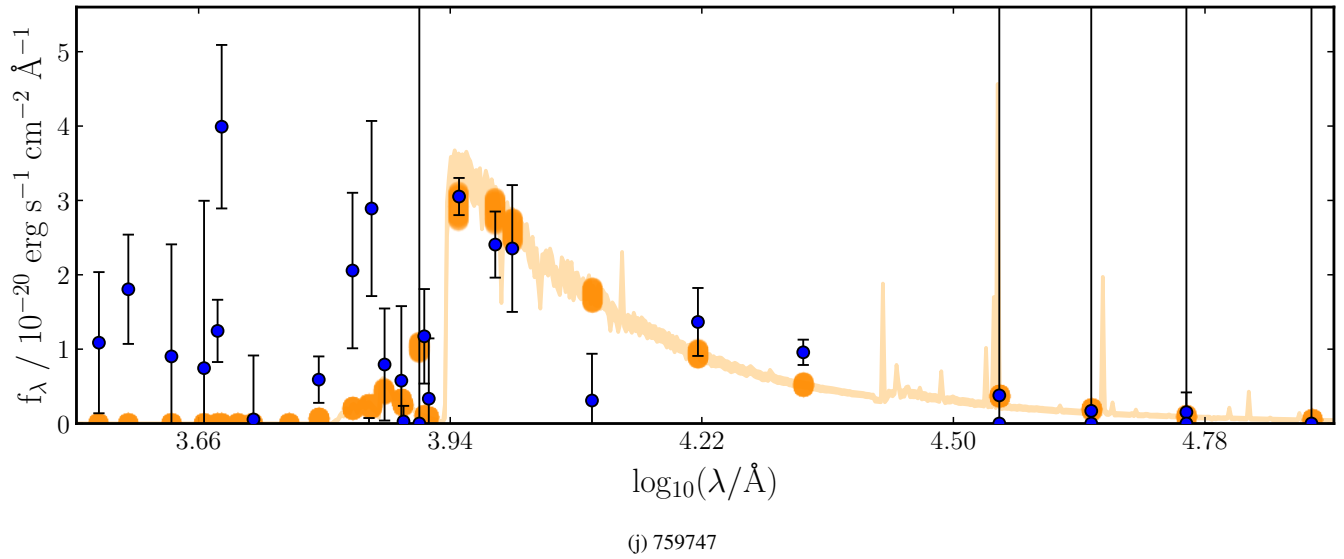


Figure D1. BAGPIPES SED fit to our protocluster galaxies. The large error bars on some data points are non-detections.